AIAA-95-3112

Velocity Fields of Axisymmetric Hydrogen-Air Counterflow Diffusion Flames from LDV, PIV, and Numerical Computation

G.L. Pellett, NASA Langley Research Center, Hampton, VA

L.G. Wilson, Lockheed Engineering and Sciences Co., Hampton, VA

W.M. Humphreys, Jr., S.M. Bartram, L.R.Gartrell, NASA Langley Research Center, Hampton, VA

and

K.M. Issac, University of Missouri-Rolla, Rolla, MO

AIAA 31st Joint Propulsion Conference

July 10-12, 1995 / San Diego, CA

Velocity Fields of Axisymmetric Hydrogen-Air Counterflow Diffusion Flames from LDV, PIV, and Numerical Computation

Gerald L. Pellett,*
NASA Langley Research Center, Hampton, VA 23681

Lloyd G. Wilson,†
Lockheed Engineering and Sciences; Hampton, VA 23666

William M. Humphreys, Jr.,* **Scott M. Bartram,**¤ **Luther R. Gartrell,***
NASA Langley Research Center; Hampton, VA 23681

and **K. M. Isaac**§
University of Missouri-Rolla; Rolla, MO 65401

Abstract

Laminar fuel–air counterflow diffusion flames (CFDFs) were studied using axisymmetric convergent-nozzle and straight-tube opposed jet burners (OJBs). The subject diagnostics were used to probe a systematic set of H_2/N_2–air CFDFs over wide ranges of fuel input (22 to 100% H_2), and input axial strain rate (130 to 1700 1/s) just upstream of the airside edge, for both plug-flow and parabolic input velocity profiles. Laser Doppler Velocimetry (LDV) was applied along the centerline of seeded air flows from a convergent nozzle OJB (7.2 mm i.d.), and Particle Imaging Velocimetry (PIV) was applied on the entire airside of both nozzle and tube OJBs (7 and 5 mm i.d.) to characterize global velocity structure. Data are compared to numerical results from a one-dimensional (1-D) CFDF code based on a stream function solution for a potential flow input boundary condition. Axial strain rate inputs at the airside edge of nozzle-OJB flows, using LDV and PIV, were consistent with 1-D impingement theory, and supported earlier diagnostic studies. The LDV results also characterized a heat-release hump. Radial strain rates *in the flame* substantially exceeded 1-D numerical predictions. Whereas the 1-D model closely predicted the max / min axial velocity ratio in the hot layer, it overpredicted its thickness. The results also support previously measured effects of plug-flow and parabolic input strain rates on CFDF extinction limits. Finally, the submillimeter-scale LDV and PIV diagnostics were tested under severe conditions, which reinforced their use with subcentimeter OJB tools to assess effects of aerodynamic strain, and fuel/air composition, on laminar CFDF properties, including extinction.

*Research Scientist (member AIAA) , NASA Langley Research Center, Hampton, VA 23681

¤Laser Applications Specialist, NASA Langley

†Research Technician, Lockheed Engineering and Sciences

§Associate Professor (member AIAA), Dept. Mechanical and Aerospace Engineering and Engineering Mechanics

Nomenclature

a_{air} = - $(du/2dx)_{edge}$, applied stress rate (ASR) along centerline of air jet, at airside edge of flame; approximated by U_{air}/D_n for nozzles; and proportional to U_{air}/D_t for tubes; 1/s.
D_n = nozzle exit diameter, cm.
D_t = tube exit diameter, cm.
K_{air} = - $(du/dx)_{edge,LV,PIV}$, measured axial strain rate along centerline, at airside edge; approximately $2U_{air}/D_n$ for a nozzle OJB, 1/s.
$K_{air,LV}$ = $2U_{air,LV}/Dn$, based on LDV.
$K_{air,MF}$ = $2U_{air,MF}/Dn$, based on Mass Flow.
r = radial coordinate, cm.
R = correlation coefficient, least-squares fit.
Re = Reynolds number based on jet exit.
u = local axial velocity, cm/s.
$u_{min,air\ edge}$ = minimum axial velocity near air edge of flame.
$u_{max,flame}$ = maximum axial velocity in flame.

U_{air} = cross-section-average air velocity at jet exit; MF is calibrated at 0 °C and 1 atm, cm/s.
$U_{air,LV}$ = U from LDV measurement.
$U_{air,300K,MF}$ = U from Mass Flow at 300 K.
v = radial velocity, cm/s.
x = axial coordinate, cm.
$X(i)$ = mole fraction of species i, input jet.

Introduction

For several years the authors have conducted experimental studies on aerodynamically-strained laminar fuel– (versus) air counterflow diffusion flames (CFDFs), using various axisymmetric opposed jet burners (OJBs) and combustion diagnostic techniques.[1-12]. Extinction results were presented earlier for respective H_2/N_2–clean air, H_2/N_2–contaminated air, and H_2/hydrocarbon–air systems. This paper contains newly obtained diagnostic results from two non-intrusive techniques used to probe a systematic set of strained H_2/N_2–air CFDFs. Laser Doppler Velocimetry (LDV) and Particle Imaging Velocimetry (PIV) were applied to CFDFs to characterize their global velocity structure. The experimental methodology and data characterizations are assessed in light of earlier pioneering studies of counterflow flames [13-26], and also more recently published experimental, analytic and numerical results.[27-51]

Laminar disk-shaped CFDFs were formed when a H_2/N_2 fuel stream jet was opposed by a similar air stream, using axisymmetric convergent-pyrex-nozzle OJBs (7.2 and 5.1 mm i.d.), and also long straight tube OJBs (7.0 and 5.0 mm i.d.). To aid the discussion, schematic diagrams of a typical nozzle-OJB system (detailed later), and the resultant axial and radial flowfields of a CFDF, are shown in Figs. 1a and 1b. The gap between opposed jets was set at two exit diameters, so the flame was always unanchored, and hence free-floating when input flow rates were changed slightly. The strained combustion flow-fields measured by LDV and PIV represented widely variable temperature, composition, and velocity fields. The measurements were compared with numerically evaluated velocity and temperature profiles obtained using a comprehensive one-dimensional (1-D) model [11] for CFDFs.

The objectives of this study were to increase fundamental understanding of the airside flow field of strained H_2/N_2–air CFDFs, and to assess applicability of the subject diagnostic techniques. The flowfield information is needed to validate detailed 1-D and 2-D numerical models of laminar counterflow flames. More generally, the CFDF results may contribute to improved (a) applications of laminar flamelet theory and other subgrid models used to characterize turbulent non-premixed combustion; (b) analysis of flame-holding processes at various temperatures and pressures in hydrogen-fueled high-speed airbreathing engines, and control of diffusive H_2 combustion in boundary layers; and (c) reduction of combustion uncertainties associated with use of contaminated high-enthalpy air in ground test facilities.

Background

The present authors, and many other investigators, have examined various aspects of flame structure, strain-induced extinction, and chemical kinetics of idealized counterflow flames. Most experimental studies by others have concentrated on simple hydrocarbon-air systems, such as methane–air, at relatively low strain rates. [27-33,36,37,44,45,47]

The uniqueness of the H_2–air system requires special considerations. First, the very low flammability limit of H_2 in air, and relatively rapid diffusion of H_2 and H atoms, causes the flame zone edge to locate on the airside;[15] e.g., for the current experiment the authors estimate a range of 0.2 to 8 mm upstream of the stagnation point, depending on axial input strain rate (2000 to 100 1/s) and input H_2 concentration (20 to 100%). Thus diffusive combustion proceeds in a strained laminar flame structure,[15,18-22,24,27] through which air and combustion products flow. Second, very high strain rates are needed to reach conditions that even approach extinction; e.g., H_2–air extinction requires 28 times higher strain rates than CH_4–air.[10,12]

Because radial strain rate varies as jet velocity divided by diameter, U/D, and Re varies as U times D, the use of small nozzles and tubes allows relatively high strain rates to be achieved while maintaining laminar flow over the impingement region -- this allows for more exact numerical modeling of CFDFs. In turn, these small jet diameters necessitate relatively wide nozzle and tube separations (≥ 2 D), to assure that finite thickness flames are

always centered far enough from the jets to be free-floating; i.e., unanchored by heat and/or radical loss mechanisms, and free from an imposed axial velocity gradient that is modified by combustion. These requirements contrast with the sometimes idealized combination of relatively-large closely-spaced nozzles, which satisfy the mathematical simplicity of an infinite-diameter assumption. Such nozzles are frequently used in diagnostic studies of lightly strained flames, and for extinction of much weaker flame systems than 100% H_2–air. [28-36]

The author's preferred input flow parameter for a strained CFDF has been the air jet exit velocity, U_{air} (cross-sectional-average, standardized at 0 °C and 1 atm). The U_{air} at extinction has recently been defined as "flame strength" (FS) by the authors.[10,12] Note, parenthetically, that Potter pioneered the tube-OJB, and defined the term "apparent flame strength" as average mass flux of fuel and air jets at extinction.[14,16,17] Such usage may be most appropriate in hydrocarbon systems, where fuel and air molecular weights and transport properties are more similar, and the counterflow flame is located closer to the stagnation point. From a practical viewpoint, U_{air} in the hydrogen–air system represents the velocity at which a specific counterflow stagnation flame processes incoming air. At extinction, U_{air} attains a maximum and the flame fails catastrophically -- due to increasing heat loss, falling temperature, and decreasing reactivity in the flame.

If U_{air} is normalized by OJB diameter, the applied stress rate (ASR) at the airside edge [37] is *approximated* for finite nozzles by $a_{air} = U_{air}/D_n$; however, for tubes, ASR is only proportional to U_{air}/D_t, and estimation of the empirical proportionality factor (~3)[10,12] is one subject of the PIV and LDV investigations. Based on application of 1-D theory [37] to impingement of *constant density (e.g. cold), finite-diameter*, uniform axial jets (plug flow),[21,52] a_{air} should approximate one-half the axial strain rate $(-du/2dx)$ at the outer airside edge of the boundary layer, and also radial strain rate (dv/dr) near the stagnation point. Note, however, that combustion can substantially alter the actual radial and axial strain fields within the impingement flame. In subsequent sections, the input axial strain rate at the airside edge, $K_{air} = 2a_{air}$, will be approximated through use of OJB exit diameter, and jet input velocities derived from LDV, PIV, and mass flow measurements.

Various non-intrusive laser diagnostic techniques were previously applied to strained hydrogen–air diffusion flames. These included use of a 7.0 mm tube OJB to obtain limited characterizations of: (a) temperature and composition fields of H_2/N_2–air CFDF, using Coherent AntiStokes Raman Spectroscopy (CARS) [6] and Laser UV Raman techniques;[38,39] and (b) axial and radial velocity fields on the airside, using Laser Doppler Anemometry (LDA).[6,40,41]

In this paper, extensive LDV and PIV studies were conducted, using a commercial three-axis LDV system, and a specially designed PIV system consisting of double-pulsed Nd-YAG lasers.[12,53-55] Both alumina and hollow silica particle (microfeathers) seeding were used on the airside of both nozzle and tube OJBs. Initial objectives were to demonstrate that (a) input axial velocities in the cross-sectional plane exhibit plug-flow or top-hat profiles for nozzles, and parabolic profiles for tubes; and (b) progressive changes in axial and radial velocity distributions in the axial direction represent the main characteristic of free-floating jet impingement, with concomitant conversion of axial-to-radial strain rate.

The scientific and practical relevance of H_2–air CFDFs, and particularly those near extinction, can be examined from various viewpoints. First, the literature strongly suggests that strain-induced extinction of 100% H_2–air CFDF should be rate-controlled by chemical kinetics in the airside flame, even though hydrogen is transported to the airside by diffusion.[15,27,37,45-51] This should also apply to N_2-diluted H_2 fuels, down to a certain H_2 concentration range. Below this critical range (~80% H_2 [10]), extinction limits should also be sensitive to decreased H_2 and H atom diffusion caused by inert diluent. Second, a primary advantage of axisymmetric CFDFs is that a relatively uniform radial strain rate *should* exist along any planar isothermal surface located in the impingement flame region [37] (CFDFs examined in this study were previously found 1-D in the central region via focusing schlieren [12]). Thus the OJB should be particularly useful for measuring a macroscopically-uniform (non point source) strain rate over a range of conditions.

The limited applicability of numerical CFDF models, for practical input boundary conditions, continues to impact the use of OJB systems. The two existing comprehensive numerical models for axisymmetric opposed jet flows are one-dimensional (1–D) and apply only along the axial streamline. These models represent similar boundary-layer approximations, but stem from two different Navier-Stokes stream function solutions.[37] They apply to either (a) a potential flow input condition (i.e. diverging flow from a distant point source), used first in Ref. 45 and then by several other researchers; or (b) a plug flow input from closely-spaced large-diameter jets, developed first in Ref. 47 and then used by others. Potential flow inputs have been used to evaluate the characteristics of methane–air and H_2–air CFDFs up to extinction. However, plug flow solutions have only been successful for methane–air [33,37,47] until recent studies of the 100% H_2–air system.[51]

Unfortunately, even the latter 1-D plug flow solution [51] cannot be used to analyze the present H_2–air nozzle-OJB flows, due to the small jets required for laminar flow, and the proportionately large gap used to prevent flame anchoring. The missing link is either (a) detailed experimental knowledge of an effective (or virtual) jet gap for each unanchored flame, and/or (b) an independent analytic/empirical expression for input axial strain rate, based on exit velocity, fluid properties, and nozzle diameter. Thus, because suitable 1-D or (preferably) 2-D numerical models have not been developed to accomodate *either* plug flow *or* parabolic input profiles for the present systems, experimental composition, temperature, velocity, and extinction measurements derived from nozzle- or tube-OJBs cannot be compared *exactly* with any known numerical results. Very recently a 2-D axisymmetric model has become available,[57] so the effects of input velocity profile and H_2 input concentration can, in principle, be fully examined in 2-D space.

In summary, the present investigation is designed to compare high strain rate laminar flames to calculations and theory. Detailed information on jet input velocity profiles, and resultant strain rate fields, is needed to validate numerical codes, make comparisons with independent results of other researchers, and support development of sub-grid models for efficient high speed combustion.

Experiment and Analysis

The LDV and PIV techniques were applied to a comprehensive set of OJB flames which varied systematically in input composition, from 22 to 100% H_2, and input axial strain rates from 130 to 1700 1/s.

Opposed Jet Burner: Referring to Fig. 1a, axisymmetric opposing laminar flows of fuel and air mixtures were formed either by matched pairs of long pyrex tubes (5.0 and 7.0 mm i.d., and 100 to 50 diameters long), or convergent pyrex nozzles (5.1 and 7.2 mm i.d.). The pyrex nozzles were fabricated by vacuum-forming heat-softened pyrex over smooth machined graphite mandrels; excess length of pyrex at the nozzle exit was trimmed with a diamond saw. This technique helped produce smooth and reproducible nozzle interior walls. Convergence occurred over a short distance (1:1 aspect ratio), the contraction ratio was 10:1 by area, and the nozzle exit was "recurved" in a short ($D_n/2$) straight-walled flow-straightening section.

The OJB tubes and nozzles were mounted vertically. The upper fuel element was well insulated to prevent convective heating of the pre-emergent fuel caused by a conical sheath of hot flame gases. The lower air element was not insulated. Subsequent independent measurements of input air temperatures in the upstream supply, and in the nozzle throat using shielded thermocouples, indicated that air flows were moderately preheated in a systematic, empirically-described fashion. The OJB jets were separated by two exit diameters, which was previously shown to avoid flame anchoring processes for all flames studied.[10,12] Previous extinction limits obtained from 7 mm tube-OJBs in the horizontal orientation, and vertical fuel-on-top and air-on-top configurations, were virtually identical; pre-extinction 7 mm tube flows of fuel and air differed only a few percent due to small differences in flame curvature induced mainly by misalignment of tubes.[6] Thus, at the flowrates used, buoyancy had negligible effect on the extinction and jet momentum balance of centered flames.

The typical nozzle-OJB system, Fig. 1a, was enclosed in a box made of porous ceramic fiber material (25 mm thick), with a porous top of sintered metal or ceramic fiber, and four Pyrex windows. Argon entering at the bottom of

the box prevented or inhibited extraneous combustion outside the central impingement region, and thus minimized adverse buoyancy and visibility effects. Fuel and air component flows were hand-controlled with micrometer valves, and measured by mass flowmeters calibrated at 0 °C and 1 atm. The reported area-average jet velocities, U_{air} and U_{fuel}, were calculated from component mass flows and measured OJB exit diameters. The resultant U_{air} data were referenced to 300 K (ideal gas law), unless otherwise noted, regardless of actual jet temperature.

Seeding System: Several types of seeding apparatus and refractory seed material were used during the two sets of PIV tests (pre- and post-1994), because agglomeration processes tended to produce unacceptedly large particles. Large agglomerates not only failed to track the gas flows in regions of steep velocity gradient, due to excessive inertia, but with PIV they tended to dominate light scattering and cause small particles to pass unrecorded.

During the pre-1994 tests, Union Carbide Linde C alumina seed (aerodynamic size ~ 1.0 micrometers) was dispersed from the bottom of a cylinder by downward-directed air jets, and "scrubbed" by a leather piston collar.

During the post-1994 tests the seeding system was replaced. The same Linde C alumina was used for a while, and then the alumina was replaced by very low density (0.45 g/cm^3), but expensive ($25/gram), hollow silica microspheres, to improve particle tracking response. The replacement seeder consisted of a three liter polyethylene bottle with a high speed motor-driven propeller mounted in the bottom. The aerodynamic particle sizes for both seed materials were obtained using a TSI® APS instrument, and the normalized size distributions are shown in Fig. 2. Although the peak count for silica spheres occurred at somewhat larger size, the 5x reduction in particle density allowed a major improvement in tracking.

An unique air delivery system was also developed, consisting of twin solenoid-activated valves to control air bypass, and twin mechanically-joined micrometer valves that simultaneously throttled input flows to the seeder *and* the bypass air line. Thus the limited, expensive supply of silica seed could be delivered at a controlled rate for just a few seconds, without significant waste during interim bypass.

Laser Doppler Velocimetry (LDV): The LDV used for this test was an orthogonal three-component system, composed of 1-D and 2-D commercially available fiber optic probes. The illumination source was a 5 watt (all lines) Argon ion laser. The 514.5 nm (green), 488 nm (blue) and 476.5 nm (violet) wave lengths were assigned to the axial (u), radial (v) and tangential (z) velocity components, respectively. The LDV fringe spacing and spatial resolution were ~2.0 and ~70 microns, respectively. Color separators were used to distinguish the individual velocity components. The period of input Doppler burst frequency was measured using counter-base digital signal processors with 1.0 ns resolution. These signal processors were equipped with features that rejected extraneous noise caused by the occurrence of multiple particles in the measurement volume, and the high pedestal signal applitudes produced by large particles. A master interface unit was used to multiplex the output of the signal processors to a microcomputer, and the velocity data were stored on disk.

Ensembles of velocity data were typically acquired for about 3 to 5 s, and then averaged at each axial measurement location along the centerline. Longer acquisition times occurred near the stagnation point where the data rate tended to fall off. The position of the flame edge was verified during data acquisition by visual sighting against a background target. The LDV fiber optic probes were mounted on a traversing system that had a 10 micron step resolution.

Axial, radial, and tangential velocities were measured in the region between the air nozzle exit and the stagnation plane. The air side was seeded using nominal 1 micron alumina particles. To minimize disturbance to the flame, the flow field was initially seeded to levels that allowed the seeding apparatus to be turned off during data acquisition, while sufficient particles stayed resident within the airside flow. Typically, 1000 velocity ensembles were averaged for each measurement location in the axial direction. Successive measurements were typically ~1 minute apart.

Because LDV measures velocity of individual particles, measurement accuracy depends strongly on how well these particles track the flow. The severity of particle inertial and thermophoresis effects [61,62] depends on particle density, size and shape, and local strain rates and temperature gradients, as discussed later.

Additional errors arose from the cross beam measurement, the electronics, and measurement uncertainties due to the statistics of the velocity ensemble. The cross beam angle measurement uncertainty (bias error) was ±1.5 percent. The electronics errors caused by quantizing and clock synchronization were negligible due to the relatively low Doppler frequency (1 Mhz) in comparison to the signal processor reference clock (1 GHz). For the statistical mean of the velocity ensemble, the standard error was generally below 10 percent (detailed RMS data are shown later).

The initial axial scan position was referenced to the edge of the nozzle on the air side of the OJB. Step sizes of 0.5, 0.4, 0.2, and 0.1 mm in the axial direction were selected according to the input flow conditions and measurement location, with finer step sizes being used near the stagnation region.

Particle Imaging Velocimetry (PIV): The system used to collect global air jet velocity information utilized a traditional double-laser-pulsed photographic PIV technique to image the airside flow field, which was seeded with light scattering particles.[12,53-55]

PIV Data Acquisition: The PIV data acquisition system, shown schematically in Fig. 3a, utilized two frequency-doubled, 300-mJ Nd:YAG lasers, which generated a double-pulsed vertical light sheet approximately 2 cm high and 1 mm thick. This light sheet bisected the OJB along the axial centerline. A 70-mm camera system using Kodak Tri-X film photographed the light sheet during laser firing, thereby capturing particle images in the illuminated air jet flow.

To overcome an image overlap problem that occurs in the region of stagnation flow, a unique rotating mirror system was added to the optical path in front of the 70-mm camera. This allowed introduction of an artificial image shift on the photographs.[57,58] The image shift was adjusted to ensure that zero or negative velocities would produce a positive image displacement of the second particle image with respect to the first. Thus the displacement would occur in the same Cartesian quadrant and would be large enough to prevent image overlap. By subtracting out the image shift during photograph interrogation and data processing, zero velocity and flow reversals could be easily detected.

Another unique feature of the PIV measurements was the use of 3X image magnification to increase spatial resolution of the photographs to the submillimeter range. The large magnification required engineering trade-offs. First, the resultant f-number was larger, and this required use of faster and relatively grainy films. Second, because photographed particle image sizes were directly proportional to camera magnification, the larger image sizes tended to increase the uncertainty of velocity measurements -- an effect observed during subsequent analyses of reduced PIV data. However, by carefully controlling the focus and f-number of the camera system during data acquisition, this uncertainty was minimized.

System Calibration: Calibration of the PIV system consisted of accurately measuring the laser pulse separation, the magnification of the camera system, and the induced image shift of the rotating mirror system. The laser pulse separation was obtained by diverting a portion of the output beam from each laser to a photodiode connected to a digital oscilloscope. Measurement of the camera magnification was achieved by photographing a reticle placed in the plane of the light sheet. The reticle contained a precision chrome-on-glass etching of a rectangular grid of lines, with 0.25 mm grid spacing. Photographs of the reticle were analyzed to measure the grid spacing on film. Comparison of this spacing with the actual reticle spacing gave an accurate measurement of the camera magnification. Finally, the induced image shift of the rotating mirror system was measured by photographing a glass plate sprayed with particles and placed in the plane of the light sheet. The lasers were then double pulsed and a photograph obtained. The resultant image displacements were directly attributable to the induced image shift, since there was no motion associated with the glass plate. In this manner the image shift could be measured to within a few micrometers.

Photograph Analysis: The entire airside flow field was characterized for several OJB test conditions, using several photographs obtained for each condition. Generally, out of each ensemble of photos for a particular flow condition, only the highest quality photograph was selected for analysis. This photograph was placed in an interrogation system, Fig. 3b. The system imaged overlapping square regions of

the photograph (approximately 3 mm on a side with a 1.5 mm overlap) onto a CCD camera connected to a frame buffer. The frame buffer system digitized and mapped these interrogation regions to a 512 x 512 pixel grid with 8-bit resolution. Fourier-based spatial autocorrelation analysis of the resultant intensity distribution was then performed to ascertain the average particle image displacement, and thus the flow velocity, corresponding to the interrogation region. The image shift induced by the rotating mirror system was removed at this point to determine actual flow directions. Once the entire velocity field was obtained, the data were manually inspected to remove any erroneous vectors, and a linear interpolation process was performed to fill any gaps in the velocity field. Finally, the axial velocity gradient in the vicinity of the jet centerline, and the radial velocity gradient in the vicinity of the stagnation region, were computed from the velocity field.

Numerical Modeling: The 1-D numerical model used for comparisons in this paper was recently developed to predict the flame structure and strain-induced extinction limits of hydrogen-air CFDF.[9,11,43] The model was formulated by reducing the governing equations to a spatially 1-D set, and employing a traditional similarity transformation that applies strictly to a finite impingement boundary layer. The ordinary differential equations were written in time-dependent form, and solved by a time-marching, finite-volume technique. A special treatment of the species production term, by subdivision into creation and destruction terms, alleviated difficulties associated with numerical stiffness of the equations due to the high hydrogen reaction rates and molecular diffusion. The complete model included detailed thermodynamic and transport property sub-models, thermal diffusion (found unimportant), and a multi-step chemical mechanism based on 7 species (H_2, O_2, H_2O, H, O, OH, and HO_2) and 22 reactions.

Note, because the present model was developed independently of a previous family of 1-D models that use the potential flow input boundary condition for H_2–air,[37,45-46,48-49] the model has served as an independent comparison-check with other numerical results (ICASE Workshop on Combustion, NASA Langley, June 1993). In fact, the authors recently identified the occurrence of a so-called "low strain rate catastrophe," which can begin to exhibit anomolous behavior at strain rates << 100 1/s. Thus an application can exceed thin-boundary-layer limits for 1-D models, in which the radial derivatives of composition and temperature are assumed negligible.

1-D CFDFs & Previous Focusing Schlieren: The degree of one-dimensionality of the previous and present H_2-based CFDFs, due to the preferred 2:1 nozzle gap-to-diameter ratio used, has been a possible cause for concern regarding (a) the accuracy of previous extinction results obtained from the 7.2 mm nozzle OJB, and (b) the validity of comparisons with numerical results from 1-D codes. As stated earlier, most researchers who study lightly strained flames use large diameter tubes, placed close together, and filled with mesh to reduce turbulence. Such setups have inherent disadvantages, such as limited strain rate range, microturbulence, and the possibility of tube walls acting as heat/radical sinks and/or adversely influencing the flow field. The present OJB does not suffer these potential shortcomings. The degree of one-dimensionality of the resultant CFDF thermal zones was demonstrated earlier using focusing schlieren,[12] based on detailed surveys over a wide range of input conditions. It was concluded that the flame zone and hot gas flow field were effectively 1-D for the central 5 to 7 mm of a 7.2 mm Pyrex nozzle OJB system (and out to much larger radii for higher strain rates). This was the largest diameter, and thus most ideal nozzle OJB used.

LDV Results and Discussion

The LDV axial velocity profiles were obtained in sequential steps along the centerline, from the air nozzle edge, for CFDFs formed by plug flow inputs using the 7.2 mm nozzle OJB. Thirteen high-resolution profile sets (0.2 and 0.4 mm interval), and 44 low-resolution sets (0.5 mm), were obtained. Analyses of the profiles led to several 1-D characterizations and comparisons with 1-D numerical results. The H_2 input range varied from 22 to 100 mole percent, and axial strain rate inputs varied from 130 to 1700 1/s. Note, although each data set applied for a fixed input, the individual meas-

urements were sequential (~1 minute apart) and hence quasi-independent. Thus any flame shift during or between determinations could cause an error in the axial velocity distribution.

The thirteen high-resolution LDV profiles are shown in Fig. 4a-d for H_2 inputs ranging 1 to 4 standard (at 0 °C) liters per minute (SLPM). Whereas *all* profiles started at the air nozzle edge, the profiles are shifted axially for clarity. Resultant H_2 input concentrations ranged 29 to 84%; and the input axial strain rate, approximated by $K_{air,LV} = 2U_{air,LV} / Dn$, ranged 173 to 1437 1/s.

Before proceeding with detailed analyses, Figs. 5a and 5b show corresponding axial distributions of RMS velocity fluctuations for the two extreme (first and last) cases in Figs. 4a-d (83.5% H_2 at 173 1/s, and 33.2% H_2 at 1437 1/s). In the first case, RMS fluctuations increased somewhat within the flame zone. In the second case, RMS fluctuations were about 3 to 4 times larger, but the mean axial velocities were up to 8x larger. Thus the RMS variations, coupled with the other two LDV components, indicated that flows were laminar throughout.

Axial Strain Rate at Airside Edge: Axial strain rate inputs, $(du/dx)_{LV}$, were measured for the 13 cases using least-squares linear fits of LDV data just upstream of the relative minimum on the airside (typically 6 to 10 points). Resultant slopes are plotted on a log-log scale in Fig. 6a as a function of $K_{air,MF}$, deduced from mass flows and nozzle diameter for an assumed 300 K, using $2U_{air,300K,MF} / D_n$. These LDV strain rates are a factor of 1.5 higher than the idealized proportionality (bold line), but the slope is approximately unity (1.01), indicating direct proportionality with applied stress based on mass flows. Essentially identical results were also obtained for the low-resolution LDV data, which are combined with the high-resolution data in Fig. 6b.

However, when $K_{air,LV}$ was deduced from LDV-measured input air velocities, using $2U_{air,LV} / D_n$, and substituted as the abscissa, Fig. 6c, most of the offset was removed. Although the slope was slightly less ideal (1.17 for high-resolution, and 1.15 for combined data), the strain rates more closely fit idealized 1-D impingement theory. Thus Fig. 6c clearly illustrates the successful use of measured axial input velocities, $U_{air,LV}$, to *approximate* axial strain rate input at the airside edge of the flame, in accordance with the idealized cold flow impingement model. It is concluded that the input flowfield for the 7.2 mm nozzle OJB was essentially 1-D and ideal for the range studied.

Despite this ideality based on LDV data only, it also became clear that heating of the air jet -- in the exposed portion of the tube and nozzle (~80 mm) protruding into the combustion box -- had caused $U_{air,300K,MF}$ to differ systematically with $U_{air,LV}$. Thus plots of the strain rate data referenced to air mass flows at an *assumed* 300 K were not fully useful in testing the 1-D theory.

Note parenthetically that previous CARS data on a 7.0 mm straight tube OJB did not indicate significant air heating.[6] However, the present 23 mm i.d. feed tube had a 10x longer residence time for heat-up before reaching the short tapered nozzle section and 7.2 mm exit. In addition to this study's direct confirmation of air jet heating using shielded thermocouples, independent evidence of air jet heating was also observed [42] using UV-Raman on an essentially identical OJB.

Because the exit air temperature could not be measured accurately in this study, using a nonintrusive technique, an attempt was made to determine an appropriate correction. The LDV data were analyzed to deduce an effective excess temperature, ΔT, which made $U_{air,300K,MF}$ equal $U_{air,LV}$. Fig. 7 shows the resultant ΔT as a function of $2U_{air,300K,MF} / D_n$, for both the high- and low-resolution LDV data grouped according to input H_2 mass flow rate (1,2,3,4 SLPM). The respective 1 and 4 SLPM data sets agreed exceptionally well, whereas those for 2 and 3 SLPM differed slightly. The excess heating depended inversely on airside applied stress (or directly on residence time), *and* it also depended on H_2 flow rate, which influenced heat release in the combustion box. Using respective high-resolution data at three different input H_2 concentrations, $X(H_2)$, the excess heating varied as $K_{air,MF}^{-0.40}$ at each of these fixed $X(H_2)$.

A master correlation of the high-resolution data, Fig. 8a, indicates an excellent unity-slope power-law fit, using the above strain rate function times $X(H_2)^{0.7}$. The entire LDV data set was then analyzed in Fig. 8b using the same power-law correlation. The resultant slope of unity, and the good agreement between high- and low-resolution data, indicate positive

consistency between the data sets. Finally, the limited set (15) of measured excess temperatures, derived from shielded thermocouples in the air jet, were also consistent with Fig. 8b.

In conclusion, although excess heating of the air jet was an undesirable complication, it occurred in a systematic fashion, and was successfully quantified. Excess temperatures above 300 K were deduced by assuming that mass-flowmeter-derived velocities were equivalent to LDV air jet velocities. The empirical expression is useful for conversion of standard mass flow data to velocity data, if needed. The end result is a positive confirmation of idealized input strain rates for the 7.2 mm nozzle, corresponding to 1-D impingement.

Maximum Velocity, Heat Release Hump: Inspection of the high-resolution LDV profiles in Figs. 4a-d indicates a dramatic decrease in the height, width and relative size of the "heat release hump" with decreasing input H_2 concentration *and* increasing input strain rate. The axial distance between the relative minimum velocity, $u_{min,air\ edge}$, and zero velocity at the stagnation point, is termed the "velocity hot-layer (VHL) thickness." The maximum axial velocity for the heat release hump, $u_{max,flame}$, and its corresponding thickness, are evaluated below and compared later with numerical results.

The ratio of $u_{max,flame}$, at the top of the heat release hump, to the maximum axial input velocity, $U_{air,LV}$ (~ 1 mm from nozzle exit), was evaluated for all the high-resolution runs. The results, shown in Fig. 9a as a function of input H_2 concentration, indicate that strain rate was also an important variable. Power-law fits of data for each of three input H_2 concentrations yielded respective values for {exponent, % H_2} of {-0.51, 67%}, {-0.54, 50%}, and {-0.43, 29%}. Using -0.50 to represent the average exponent (slope) on a log-log plot, the ratios were fitted by an empirical power-law expression with unity slope, as shown in Fig. 9b. These data were very well characterized by the expression,

$$u_{max,flame} / U_{air,LV} = c\ X(H_2)^{1.2}\ [K_{air,LV} / K_o]^{-0.5}$$

where $c = 25.7$.

Note the above experimental results cannot be compared with numerical results derived from the Heimenz potential flow input boundary condition, because input strain rate, $(du/dx)_{edge}$, is constant for the model, and $U_{air,LV}$ is not. However, the ratio of $u_{max,flame}$ to $u_{min,air\ edge}$, and also the apparent thickness of the velocity hot layer, can be obtained from numerical results, as shown in the following section.

1-D Numerical -- LDV Comparisons: Numerical results were generated, corresponding to the 13 high-resolution LDV cases, by specifying input H_2 concentration, and applied stress input estimated by $U_{air,LV} / D_n$. Results included 1-D axial profiles of the concentrations and production / destruction rates of the seven species, and corresponding temperature and axial velocity profiles. Example profiles of H and O atoms, OH and HO_2 radicals, and respective production and destruction rates, are given elsewhere.[11] The presently evaluated temperature and velocity profiles are shown in Figs. 10a-e for 5 of the 13 cases. In these plots zero axial position marks the stagnation point (SP). To allow comparisons, the LDV data were transposed and translated so that $u_{min,air\ edge}$ was approximately aligned for both numerical and LDV experimental results.

For dilute H_2 inputs the numerical temperature profiles are nearly symmetrical about the stagnation point, even though onset of the airside flame occurs more than 1 mm upstream. Results at progressively higher input H_2 concentrations show much greater asymmetry about the stagnation point, e.g. the temperature profile is almost entirely on the airside; peak temperature is much higher; and the onset of airside flame occurs up to 6 mm upstream. Finally, note that peak temperature, and full width at half peak height compared favorably with previous data correlations [12] based on similar input composition and flow parameters.

Two characterizations of the heat release hump were derived from the numerical and LDV axial velocity profiles. First, the ratio of $u_{max,flame}$ to $u_{min,air\ edge}$ was evaluated as a measure of the velocity reversal caused by the heat release. Second, the apparent velocity hot-layer (VHL) thickness was equal to the axial coordinate for $u_{min,air}$, since the stagnation point represents the origin.

As a caveat, recognize that $u_{min,air}$ does not exactly correspond to the airside edge of the flame, but it is very close. The minimum

represents a velocity reversal caused by two entirely different processes. That is, the cold input velocity declines along the centerline due to divergence of the impinging flow, and this decline is reversed by onset and rapid growth of heat release in the flame zone. Thus the airside edge of the flame zone is technically a short distance upstream of the axial velocity reversal, where oxidation of fuel begins. In the present analysis this small effect has negligible impact.

Respective numerical and LDV results for the u_{max}/u_{min} axial velocity ratio are shown in Fig. 11 versus $X(H_2)$. Also, the LDV-to-numerical results ratio is shown. In general, the 1-D model agrees quite well with the results, but the degree of agreement varies slightly with input H_2 concentration. Note, from the clustering of respective points at each value of $X(H_2)$, that axial strain rate had *no* effect on u_{max}/u_{min}, and this fact adds further support to the validity of the LDV measurements. Scatter in the numerical results was caused by readout errors in the velocity profiles, and the fact that axial strain rate input to the model was estimated by $2U_{air,LV}/Dn$, which sometimes differed from $(du/dx)_{LV}$ at the airside edge (seen in Fig. 6c).

The apparent velocity hot layer (VHL) thickness was evaluated next. The LDV data had to be extrapolated slightly, but this was not a large source of error. The numerical results, when first plotted, showed that axial strain rate *and* input H_2 flowrate (and hence $X(H_2)$ in this series) affected the VHL thickness results. Thus numerical results at fixed $X(H_2)$ were analyzed as before to determine the power-law slopes. Fits for each of the three input H_2 concentrations yielded respective values for {exponent, % H_2} of {-0.52, 67%}, {-0.51, 50%}, and {-0.50, 29%}. Clearly the 1-D numerical VHL thickness varied inversely as the square root of strain rate. Using -0.50 as exponent, the numerical Δx values were fitted by an empirical power-law expression with unity slope and c = 82.6, as follows,

$$\Delta x = x_{u,min} - x_{St} = c\, X(H_2)^{0.75}\, [K_{air,LV}/K_o]^{-0.5}$$

and the results are shown in Fig. 12.

The same power law exponents were used to analyze the LDV Δx data. The respective results in Fig. 12, indicate that both the numerical (c = 82.6) and experimental (c = 59.6) Δx results were very well characterized by the above empirical relationship. However, the numerical VHL thicknesses were ~ 1.40 times larger than the experimental results.

This 40% offset appears to represent a deficiency of the 1-D model *in the flame*. As discussed in a subsequent section, typical deviations due to particle inertial lag and thermophoresis were evaluated by Dancey et al. The net axial effect in similar flames was insignificant for 1.3 micron Al_2O_3 particles, but five micron particles led to thicker VHLs. Thus, although inertial effects would tend to increase the apparent VBL thickness at high strain rates, and thermophoresis would tend to decrease it, especially at low strain rates in steep heat-up regions, the net effect for the present axial in-flame LDV measurements (dominated by 1 micron Al_2O_3) should have been relatively small. In conclusion, the 40% increase in VHL thickness represents an overprediction by the 1-D model.

Jet Momentum Balance & Heat Release:

Axial fuel/air jet momentum ratios were determined first for the 13 high-resolution LDV cases, and then for all the LDV and PIV runs in this study. When all the ratio data from 7.2 mm nozzle-OJBs were plotted versus $X(H_2)$ there was substantial scatter; e.g. at 60% H_2, ratios ranged from 1.0 to 0.4. Upon inspection, the largest deviations from unity corresponded to the largest heat release humps. A simple explanation is that, with increased airside heat release, the impinging air jet expands and diverges more rapidly in the radial direction. In compensation, the axial air jet momentum must increase, to provide sufficient x-momentum at the stagnation plane for flame centering, and thus the fuel/air momentum ratio decreases.

Because the jet momentum imbalance resulted from the effect of heat release on axial velocity, it was logical to test a correlation of the fuel/air momentum ratio using the same abscissa that characterized $u_{max,flame} / U_{air,LV}$ for the heat release hump. The results, Fig. 13, exhibited significant reduction of data scatter and an excellent correlation of all the 7.2 mm nozzle data. Note that data in the upper left, which correspond to the most highly diluted fuel and the highest strain rate, are approximately unity. Thus the data runs that coincided best with the assumption of constant-density idealized 1-D impingement, were in fact ideal

with respect to unity axial fuel/air momentum ratio. The remaining nozzle- and tube-derived ratio data in this study, which were similarly perturbed by heat release, were also normalized very well by the same abscissa. However, a single correlation of *all* the nozzle and tube data sets appeared to require an additional function of jet diameter that extended beyond this study.

Inertial Lag, Thermophoresis Effects: To assess possible deviations in the LDV results due to particle inertial lag, the authors analyzed a series of test cases using a particle lag simulation model based on the work of Walsh [59] and Nichols.[60] The model computes the relative response of particles embedded in a gas flow. Variables taken into account were the relative Reynolds number based on the velocity difference between the gas and particle, the particle size and mass density, and the drag coefficient. Using calculated 1-D axial velocity and temperature profiles along the stagnation streamline, 5, 7, and 10 micron alumina particles were embedded in the gas flow. The particles were assigned initial velocity and temperature equal to the gas velocity and temperature at the exit plane of the jet. As shown in Fig. 14a, four different flame conditions representing H_2 inputs of 21 to 100% were simulated. The amount of particle inertial lag is greatly dependent on the flame conditions, and as expected becomes more pronounced for the more highly strained cases. Because the particle size distribution in Fig. 3 for Al_2O_3 seems to contain significant numbers of particles above 5 microns, it is reasonable to assume that some particle inertial lag error is present for these agglomerates.

Similar inertial lag calculations were performed for hollow SiO_2 particles used for some of the PIV measurements (described in next section). The results of these calculations are shown in Fig. 14b, where for clarity only a 100% H_2 condition is shown with simulated particle sizes of 1, 2, 5, and 10 micron. Because the hollow silica particles are of a much lower mass density that the alumina particles, the inertial lag effects are greatly reduced, even for particle sizes as large as 10 micron.

Similarly, Dancey and Long [41] calculated 1-D axial velocity profiles of gas along the stagnation streamline, and also embedded 1.3 and 5 micron particles in representative CFDF flowfields for 7 mm tube OJB flows. Dancey and Long included both inertial lag and thermophoresis effects in their analysis. Input axial strain rates and H_2 concentrations were 272 1/s (67% H_2) and 418 1/s (50% H_2). In both cases, 1.3 micron particles followed the gas velocity profile extremely well. However 5 micron particles showed significant lag errors. Thus, as stated above, because the net particle-related effects were to *increase* the VHL thickness, the 1-D CFDF model appears to *overestimate* the VHL thickness compared to measurements. A detailed analysis of thermophoresis effects for both particle types is beyond the present scope.

In conclusion, the high- and low-resolution LDV-derived axial velocity gradients at the airside edge showed quantitative trends consistent with a 1-D approximation of applied stress, for *finite* (7.2 mm) convergent nozzle flows. In addition, the high-resolution experimental velocity profiles provide a basic reference set for future 2-D modeling of H_2/N_2–air flames. Detailed analyses of LDV profiles, and the heat release hump, provided unique comparisons with 1-D numerical results for potential flow inputs (1-D plug flow solutions were not available). The 1-D model closely predicted the relative max / min axial velocity ratio in the hot layer, and its independence of strain rate, but overpredicted its thickness. Because the velocity gradients were extremely steep in some cases, they provided a challenging test bed for LDV, and especially PIV.

PIV Results and Discussion

The airside (only) PIV measurements led to independent evaluations of input velocity profiles, and axial and radial velocity gradients (strain rates). Fig. 15a shows a typical vector plot case for the 7.2 mm pyrex nozzle. Note, by inspection, the input axial velocities approximate plug flow, with slightly lower velocities in the central region. The effect of this small departure from idealized plug flow was readily visualized by the focusing schlieren as a slight increase in thickness of the central thermal layer.[12] Fig. 15b illustrates a typical vector plot for the 7.0 mm pyrex tube, and shows the parabolic-like input velocity profile one would expect from this configuration.

Survey plots of the radial distributions of axial input velocities confirmed the input profiles expected for nozzles and tubes. As

shown in Fig. 16a, the input plug-flow profile from a 7.2 mm nozzle had slightly high shoulders and a slightly depressed center. Input profiles from 7.0 and 5.0 mm tubes, Figs. 16b and 16c, were fit very well by parabolic curves. As shown, the PIV-measured velocities for these tubes agreed closely with the mass-flowmeter-derived $U_{air,MF}$ at 300 K. (Recall the minimal heating of tube air compared to the nozzle air inputs.)

On a case-by-case basis for each nozzle and tube data set, averaged axial velocities (over a radial slice) were used to determine a linear axial velocity gradient just upstream of the airside edge. For nozzles, the velocity vectors were averaged radially within $\pm$ 0.3D_n of the jet centerline; for tubes this was reduced to $\pm$ 0.2D_t. Fig. 17a illustrates the resultant PIV-deduced axial velocity gradients versus twice the respective applied stresses for nozzles (using $2U_{air}$) and tubes (using $4U_{air}$), estimated at 300 K from air mass flow rates, and OJB exit diameter. The high-resolution LDV strain rates are also included for comparison. These data (as before) are less scattered, they exhibit a near unity slope, and are 1.57x higher than the ideal 1:1 line.

Note that respective PIV data sets were obtained from air seeded using *both* alumina and hollow silica in the cyclone seeder. Because the hollow silica was of much lower density, and exhibited much less tendency to agglomerate than alumina, any lag in following gas streamlines due to inertial effects should have been considerably less for the silica. Notably, least-squares fits of the 7.2 mm (Al_2O_3) and 5.1 mm (SiO_2) nozzle data were practically identical, on a relative basis, in Fig. 17a (and 17b, below).

Recall earlier 1-D theory tests in Figs. 6b and 6c, which first used $K_{air} = 2U_{air,300K,FM} / D_n$ as the abscissa, for assumed 300 K air mass flows, to correlate measured $(du/dx)_{air\ edge}$ data from LDV. Now, LDV and PIV data from Fig. 17a are replotted in Fig. 17b using measured maximum input velocities to determine the abscissa, i.e. $K_{air} = 2U_{air,PIV\ or\ LV} / Dn$. The resultant PIV data plot follows the ideal 1-D theory quite well, on average (1:1 line, not shown), though the data trend is somewhat below it. The LDV data remain in the *same* relative relationship with the PIV data that occurred in Fig. 17a. Finally, note that use of $4U_{air,300K,FM} / D_t$, to calculate *twice* the applied stress for tube flows, appears to produce a reasonable merger of the tube and nozzle results. Unfortunately the data scatter, and radial averaging width for vectors, may have been too large for tubes to allow a decisive assessment of the empirical factor (4), which was closer to 6 [10,12] in earlier extinction studies.

Figure 17c illustrates the corresponding radial (transverse) velocity gradients in the vicinity of the flame-zone stagnation region, and as before, the same data are replotted in Fig. 17d using measured maximum input velocities to determine the abscissa. Generally, the central D_n (fractional) centimeters of the last three rows of vectors, prior to stagnation (see, e.g. Figs. 15), were used to determine dv/dr using linear least-squares fits. Note the pre-1994 PIV data from nozzles and tubes, and also 2-D LDV data from 7.0 mm tubes by Dancey et al.,[40,41] are consistent with the independent post-1994 results.

Based on the PIV data in Figs. 17c,d, it is clear that the radial velocity gradient in the flame zone is significantly larger than the 1:1 line representing idealized 1-D impingement, based on cold flow. This result was expected, based on Dancey's 2-D measurements on tube-OJB flows,[40,41] and Isaac's recent 2-D calculation.[56] Again, the use of $2U_{air,300K,FM} / D_n$ to estimate applied stress for a nozzle, and $4U_{air,300K,FM} / D_t$ for a tube, appears to produce a reasonable merger of the tube and nozzle results, given the previous caveat regarding radial width of vector averaging. Because temperatures in the radial direction are approximately uniform, thermophoresis effects should have negligible influence on these radial strain rates. Furthermore, because the 7.2 mm nozzle-OJB results, from Al_2O_3 seed, did not differ significantly from the 5.1 mm nozzle-OJB results, from the less dense (4.5x) SiO_2 seed, the results suggest that inertial effects did not have a significant effect on the radial velocity gradients. A more detailed analysis of the effects of a parabolic input profile on radial velocities, and the possible effects of radially-dependent combustion processes, cannot be made until more accurate 2-D data and numerical results become available. Finally, Fig. 17d shows a cross plot of the above airside axial input and radial in-flame strain rates. This plot confirms the linkage between individual input and resultant strain rates. Attempts to reduce scatter by introducing various functions of $X(H_2)$ were not successful.

Summary and Conclusions

Complementary sets of results from the LDV and PIV techniques helped to characterize the velocity structure of systematically varied H_2/N_2–air CFDF, using 7.2 and 5.1 mm nozzle OJBs, and 7.0 and 5.0 tube OJBs. The results were compared to corresponding numerical results from a detailed, independently-derived, 1-D numerical code, based on a stream function solution and a constant-density potential-flow input boundary condition. The PIV-derived axial input velocity profiles, for respective nozzles and straight tubes, confirmed the expected plug-flow and parabolic profile shapes. The LDV- and PIV-derived axial strain rates at the airside edge were consistent with 1-D cold flow theory for large uniform jets, and also with overall CFDF one-dimensionality observed in the authors' previous focusing schlieren studies. The (cold-flow) input strain rates were not affected by thermophoresis, but the PIV data showed some evidence of small inertial lag effects. Axial and radial strain rates *in the flame* substantially exceeded 1-D numerical predictions, as expected, and the velocity-based hot layer thickness was substantially over-predicted by 1-D theory. However the ratio of maximum-to-minimum axial velocities in the heat release hump were (a) independent of strain rate, and dependent only on hydrogen input concentration; and (b) in reasonably close agreement with 1-D model results. The respective effects of plug flow, versus parabolic, input velocity profiles on both axial and radial strain rates appeared reasonably close when a factor of 2.0 was used to account for the central maximum velocity associated with tube OJBs. Further 2-D data analysis, and also use of a recent 2-D numerical code, would improve this estimate.

In conclusion, respective results from two independent velocimetry techniques provided needed: (a) tests of effective one-dimensionality of the velocity structure of H_2–air counterflow diffusion flames; (b) empirical characterizations of the velocity structure of the heat release hump as functions of input H_2 concentration *and* (for hot layer thickness) inverse square root of axial strain rate at the airside edge; and (c) detailed comparisons with ideal numerical 1-D velocity fields. The 1-D model closely predicted the relative max/min velocity ratio in the hot layer, but overpredicted its thickness. The results support applications of counterflow diffusion flames as tools for evaluating effects of fuel and air composition on combustion in well-defined strain fields. Finally, unique LDV and PIV techniques were developed and applied to submillimeter scale combustion fields with steep temperature and velocity gradients.

Acknowledgements

The authors gratefully acknowledge: Dr. G. B. Northam for his insight and skillful guidance; William Sellers, III, and Dr. William Hunter for their timely assistance in supporting the extensive PIV (and LV) efforts; Mark Fletcher for making LDV measurements with Mr. Gartrell; Jun Zhao for the numerical calculations; and Professor William L. Roberts, IV, North Carolina State University, Raleigh, and Tom Brown, NASA ICASE Research Fellow from Vanderbilt University, for their insightful comments on the work. Finally Ms. Shiaomin Mou, Virginia Governor's School Student at NASA, helped prepare the final paper.

References

1. Guerra, Rosemary, Pellett, G. L., Wilson, L. G., Northam, G. B., "Opposed Jet Burner Studies of Hydrogen Combustion with Pure and N_2, NO Contaminated Air," AIAA Paper 87-0090, 11 pp., Jan., 1987.

2. Guerra, Rosemary, Pellett, G. L., Wilson, L. G., Northam, G. B., "Opposed Jet Burner Studies of Effects of CO, CO_2 and N_2 Air Contaminants on Hydrogen-Air Diffusion Flames," AIAA Paper 87-1960, 14 pp, July, 1987.

3. Pellett, G. L., Guerra, Rosemary., Wilson, L. G., Reeves, R. N., and Northam, G. B., "Combustion Rate Limits of Hydrogen Plus Hydrocarbon Fuel–Air Diffusion Flames from an Opposed Jet Burner Technique." Presented at 24th JANNAF Combustion Meeting, Monterey, CA,Oct., 1987. NASP TM-1025, Aug., 1988.

4. Pellett, G. L., Jentzen, M. E., Wilson, L. G., and Northam, G. B., "Effects of Water-Contaminated Air on Blowoff Limits of Opposed Jet Hydrogen-Air Diffusion Flames," AIAA Paper 88-3295, 10 pp., July, 1988.

5. Pellett, G. L., Comment on the paper "Structure and Extinction Limits of Counterflow Diffusion Flames of Hydrogen-Nitrogen Mixtures in Air," by G. Dixon-Lewis and M. Missaghi. In *Twenty-Second Symposium (International) on Combustion*, The Combustion Institute, Pittsburgh, PA, pp. 1469-1470, 1988.

6. Pellett, G. L., Northam, G. B., Wilson, L. G., Jarrett, O., Jr., Antcliff, R. R., Dancey, C. L., and Wang, J. A., "Opposed Jet Diffusion Flames of Nitrogen-Diluted Hydrogen vs. Air: Axial LDA and CARS Surveys; Fuel/Air Strain Rates at Extinction," AIAA Paper 89-2522, 19 pp., July 1989.

7. Pellett, G. L., Wilson, L. G., Northam, G. B., Guerra, Rosemary, "Effects of H_2O, CO_2, and N_2 Air Contaminants on Critical Airside Strain Rates for Extinction of Hydrogen–Air Counterflow Diffusion Flames." Presented at 26th JANNAF Combustion Meeting, Pasadena, CA, Oct., 1989.

8. Pellett, G. L., Northam, G. B., Wilson, L. G., "Counterflow Diffusion Flames of Hydrogen, and Hydrogen Plus Methane, Ethylene, Propane, and Silane, vs. Air: Strain Rates at Extinction," AIAA Paper 91-0370, Jan., 1991.

9. Ho, Y. H., Isaac, K. M., Pellett, G. L., and Northam, G. B., "Analysis of Hydrogen-Air Counter Flow Diffusion Flames," AIAA Paper 91-0582, 24 pp. Jan., 1991.

10. Pellett, G. L., Northam, G. B., Wilson, L. G., "Strain-Induced Extinction of Hydrogen–Air Counterflow Diffusion Flames: Effects of Steam, CO_2, N_2, and O_2 Additives to Air," AIAA Paper 92-0877, Jan., 1992.

11. Isaac, K. M., Ho, Y. H., Zhao, J., Pellett, G. L., and Northam, G. B., "Global Characteristics and Structure of Hydrogen-Air Counter Flow Diffusion Flame: A One-Dimensional Model," AIAA 94-0680, Jan.,1994.

12. Pellett, G. L., Roberts, W. L., Wilson, L. G., Humphreys, W. M., Jr., Bartram, S. M., and Isaac, K. M., "Structure of Hydrogen–Air Counterflow Diffusion Flames Obtained by Focusing Schlieren, Shadowgraph, PIV, Thermometry, and Computation. 25th AIAA Fluid Dynamics Conference, Colorado Springs, CO, June 20-23, 1994, AIAA 94-2300, June 1994.

13. Simmons, R. F. and Wolfhard, H. G., *Combustion and Flame*, **1**, 1957, pp. 155.

14. Potter, A. E., Jr. and Butler, J. N., "A Novel Combustion Measurement Based on the Extinguishment of Diffusion Flames," *Am. Rocket Soc. J.*, **29**, 1959, pp 54-56.

15. Spalding, D. B., "Theory of Mixing and Chemical Reaction in the Opposed-Jet Diffusion Flame," *ARS Journal*, **31**, 1961, pp. 763-771.

16. Potter, A. E., Heimel, S., Butler, J. N., "Apparent Flame Strength. A Measure of Maximum Reaction Rate in Diffusion Flames," *Eighth Symposium (International) on Combustion*, 1962, pp. 1027-1034.

17. Anagnostou, E., and Potter, A. E., "Flame Strength of Propane-Oxygen Flames at Low Pressures in Turbulent Flow," *Ninth Symposium (International) on Combustion*, 1963, pp. 1-6.

18. Pandya, T. P., and Weinberg, F. J., "The Structure of Flat, Counter-flow Diffusion Flames," *Proceedings of the Royal Society*, London, **279**, 1964, pp. 544-561.

19. Fendell, Francis, "Ignition and Extinction in Combustion of Initially Unmixed Reactants," *J. Fluid. Mechanics*, **21**, part 2, 1965, pp. 281-303.

20. Tsuji, Hiroshi, and Yamaoka, Ichiro, "The Counterflow Diffusion Flame in the Forward Stagnation Region of a Porous Cylinder," *Eleventh Symposium (International) on Combustion*, 1967, pp. 979-984.

21. Jain, V. K., and Mukunda, H. S., "On the Ignition and Extinction Problems in Forced Convection Systems," *Int. J. Heat Mass Transfer*, **11**, 1968, pp. 491-508.

22. Jain, V. K., and Mukunda, H. S., "The Extinction Problem in an Opposed Jet Diffusion Flame with Competitive Reactions," *Combustion Sci. and Technology*, **1**, 1969, pp. 105-117.

23. Tsuji, Hiroshi, and Yamaoka, Ichiro, "The Structure of Counterflow Diffusion Flames in the Forward Stagnation Region of a Porous Cylinder," *Twelfth Symposium (International) on Combustion*, 1969, pp. 997-1005.

24. Liu, T. M., and Libby, Paul A., "Boundary Layer at a Stagnation Point with Hydrogen Injection," *Combustion Sci. and Technology*, **2**, 1970, pp. 131-144.

25. Tsuji, Hiroshi, and Yamaoka, Ichiro, "Structure Analysis of Counterflow Diffusion Flames in the Forward Stagnation Region of a Porous Cylinder," *Thirteenth Symposium (International) on Combustion*, 1971, pp. 723-731.

26. Linan, Amable, "The Asymptotic Structure of Counterflow Diffusion Flames for Large Activation Energies," *Acta Astronautica*, **1**, 1974, pp. 1007-1039.

27. Tsuji, Hiroshi, "Counterflow Diffusion Flames," *Prog. Energy Combust. Sci.*, **8**, 1982, pp. 93-119.

28. Seshadri, K., "Studies on Flame Extinction," Ph. D. Dissertation, University of California, San Diego, La Jolla, CA, 1977.

29. Smooke, M. D., Puri, I. K., and Seshadri, K., "A Comparison Between Numerical Calculations and Experimental Measure-ments of the Structure of a Counterflow Diffusion Flame Burning Diluted Methane in Diluted Air," *Twenty First Symposium (International) on Combustion*, 1986, pp. 1783-1792.

30. Puri, I. K., Seshadri, K, Smooke, M. D., and Keyes, D. E., "A Comparison between Numerical Calculations and Experimental Measurements of the Structure of a Counterflow Methane-Air Diffusion Flame," *Combustion Science and Technology* **56**, 1987, p. 1.

31. Smooke, M. D., Seshadri, K, and Puri, I. K. "The Structure and Extinction of Partially Premixed Flames Burning Methane in Air," *Twenty-Second Symposium (International) on Combustion*, The Combustion Institute, 1988, p. 1555.

32. Seshadri, K., and Peters, N., "Asymptotic Structure and Extinction of Methane-Air Diffusion Flames," *Combustion and Flame* **73**, 1988, p. 23.

33. Chelliah, H. K., Law, C. K., Ueda, T, Smooke, M. D., and Williams, F. A., "An Experimental and Theoretical Investigation of the Dilution, Pressure and Flow-field Effects on the Extinction Condition of Methane-Air-Nitrogen Diffusion Flames," *Twenty-Third Symposium (International) on Combustion*, 1990, p. 503.

34. Seshadri, K., Peters, N., and Williams, F. A., "Asymptotic Analysis of Stoichiometric and Lean Hydrogen-Air Flames," *Combustion and Flame*, 1994.

35. Hahn, W. A., and Wendt, J. O. L., "Analysis of the Flat Laminar Opposed Jet Diffusion Flame with Finite Rate Detailed Chemical Kinetics," *Combustion Science and Technology*, **27**, 1981, pp. 1-17.

36. Hahn, W. A., and Wendt, J. O. L., "NO_x Formation in Flat, Laminar Opposed Jet Methane Diffusion

Flames," *Eighteenth Symposium (International) on Combustion*, 1981, pp. 121-131.

37. Dixon-Lewis, Graham, "Structure of Laminar Flames," Invited Lecture, *Twenty-Third Symposium (International) on Combustion*, 1990, p. 305.

38. Wehrmeyer, J. A., Cheng, T. S., Pitz, R. W., Nandula, S., Wilson, L. G., and Pellett, G. L., "Simultaneous Temperature and Multi-Species Measurements in Opposed Jet Flames of Nitrogen-Diluted Hydrogen and Air," Paper No. 29, Central States Section, The Combustion Institute, Nashville, TN, Apr. 21-24, 1991.

39. Pai, C.-Y., Yeralan, S., and Wehrmeyer, J. A., "Experimental Investigation of Strained Hydrogen-Air Diffusion Flames." Presented at Central States Section of The Combustion Institute, New Orleans, LA, March 15-17, 1993.

40. Yeo, S. H. and Dancey, C. L., "Experimental Determination of the Velocity and Strain Rate Field in a Laminar H_2/Air Counter-Flow Diffusion Flame via LDA," Fourth International Conference on Laser Anemometry-Advances and Applications, ASME Publication, Vol. 1, Aug. 5-9, 1991, pp 121-129.

41. Dancey, C. L., and Long, S. R., "Experimental Investigation of the Strain Rate Field in Stretched Laminar H_2/Air Diffusion Flames," AIAA Paper 93-3068, 10 pp., July, 1993.

42. Brown, T. M., Nandula, S. P., Skaggs, P. A., Pitz, R. W., Pellett, G. L., Roberts, W., Wilson, L. G., Isaac, K. M., "Multi-Point Measurement of Temperature and Species Concentrations in Opposed Jet Flames by UV Raman Scattering," AIAA 94-00226, Jan., 1994.

43. Zhao, J. and Isaac, K. M., and Pellett, G. L., "Nitric Oxide Formation in Strained Laminar Hydrogen–Air Counter Flow Diffusion Flames at Elevated Temperatures," Presented at Central States Section, Combustion Institute, New Orleans, LA, March 15-17, 1993.

44. Dixon-Lewis, G., David, T., Gaskell, P. H., Fukutani, S., Jinno, H., Miller, J. A., Kee, R. J., Smooke, M. D., Peters, N., Effelsberg, E., Warnatz, J., and Behrendt, F., "Calculation of the Structure and Extinction Limit of a Methane-Air Counterflow Diffusion Flame in the Forward Stagnation Region of a Porous Cylinder," *Twentieth Symposium (International) on Combustion*, 1984, pp. 1893-1904.

45. Dixon-Lewis, G, David, T., Gaskell, P. H., "Structure and Properties of Methane-air and Hydrogen-air Counterflow Diffusion Flames," *Archivum Combustionis*, **6**, No. 1, 1986, pp. 3-21.

46. Dixon-Lewis, G., and Missaghi, M., "Structure and Extinction Limits of Counterflow Diffusion Flames of Hydrogen-Nitrogen Mixtures in Air," *Twenty-Second Symposium on Combustion*, 1988, pp. 1461-1470.

47. Kee, R. J., Miller, J. A., Evans, G. H., and Dixon-Lewis, G., "A Computational Model of the Structure and Extinction of Strained, Opposed Flow, Premixed Methane-Air Flames," *Twenty-Second Symposium (Inter-national) on Combustion*, 1988, pp. 1479-1494.

48. Gutheil, E. and Williams, F., "A Numerical and Asymptotic Investigation of Structures of Hydrogen-Air Diffusion Flames at Pressures and Temperatures of High-Speed Combustion," *Twenty-Third Symposium (International) on Combustion*, 1990, p. 513.

49. Gutheil, E., Balakrishnan, G., and Williams, F. A., "Structure and Extinction of Hydrogen-Air Diffusion Flames," in *Reduced Kinetic Mechanisms for Application in Combustion Systems,* edited by N. Peters and B. Rogg, Springer, 1992.

50. Darabiha, N., and Candel, S., "The Influence of the Temperature on Extinction and Ignition Limits of Strained Hydrogen-Air Diffusion Flames," *Combustion Science and Technology*, **86**, 1992, pp. 67-85.

51. Balakrishnan, G., Ph. D. Dissertation, University of California, San Diego, La Jolla, CA, 1993.

52. Leclerc, Andre, "Deviation of a Liquid Jet by Means of a Plate Normal to the Axis of the Former Determination of the Free Surface by Electrical Analogy," Hydraulic Briefs, *La Houille Blanche*, 1950, pp. 816-821.

53. Humphreys, W.M., Jr., "A Histogram-Based Technique for Rapid Vector Extraction from PIV Photographs," *Proceedings of the Fourth International Conference on Laser Anemometry -- Advances and Applications*, Cleveland, Ohio, August 5-9, 1991.

54. Humphreys, W.M., Jr., Bartram, S.M., and Blackshire, J.L., "A Survey of Particle Image Velocimetry Applications in Langley Aerospace Facilities," AIAA Paper 93-0411, 1993.

55. Humphreys, W.M., Jr., Rallo, R.A., Hunter, W.W., Jr., Bartram, S.M., and Blackshire, J.L., "Application of Particle Image Velocimetry to Mach 6 Flows," *Proceedings of the Fifth International Conference on Laser Anemometry -- Advances and Applications*, Veldhoven, The Netherlands, 1993.

56. Zhao, J. and Isaac, K. M., "Influence of Geometry and Heat Release on Counterflow Diffusion Flames: A Navier-Stokes Model," AIAA 95-0133, Jan., 1995.

57. Adrian, R.J., "Image Shifting Technique to Resolve Directional Ambiguity in Double-Pulsed Velocimetry," *Applied Optics*, Volume 25, 1986, pp. 3855-3858.

58. Landreth, C.C., and Adrian, R.J., "Electrooptical Image Shifting for Particle Image Velocimetry," *Applied Optics*, Volume 27, 1988, pp. 4216-4220.

59. Walsh, M.J., "Influence of Particle Drag Coefficient on Particle Motion in High-Speed Flow with Typical Laser Velocimetry Applications," NASA TN D-8120, 1976.

60. Nichols, R.H., "The Effects of Particle Dynamics on Turbulence Measurements with the Laser Dopler Velocimeter," *Dissertation*, The University of Tennessee, Knoxville, 1986.

61. Gomez, A., and Rosner, D.E., "Thermophoretic Effects on Particles in Counterflow Laminar Diffusion Flames," *Combustion Science and Technology*, **89**, Nos. 5-6, 1993, pp. 335-362.

62. Sung, Chih-Jen, "On the Structure, Response, and Stabilization of Stretched Flames," *Dissertation*, Princeton University, Nov. 1994.

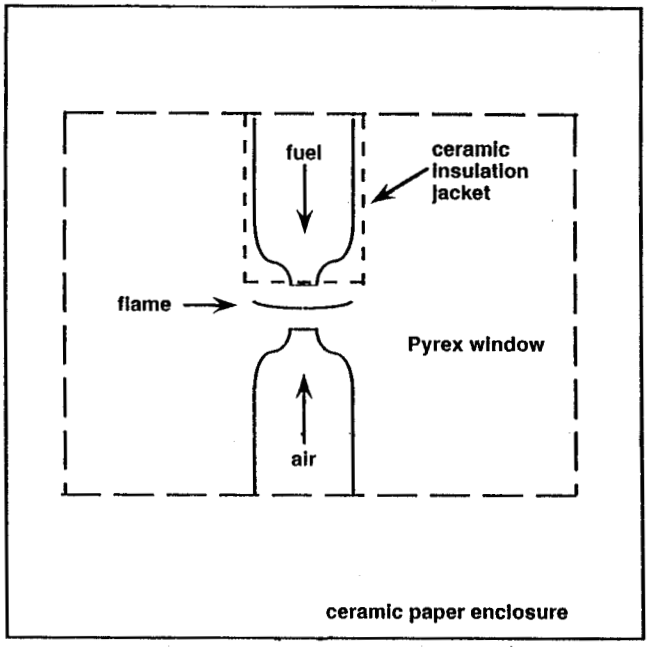

Fig. 1a. Schematic diagram of a Pyrex-nozzle opposed jet burner (OJB) oriented in the vertical direction. Nozzle exit diameters for two OJBs were 7.2 and 5.1 mm, and jet separations were 14 mm and 10 mm.

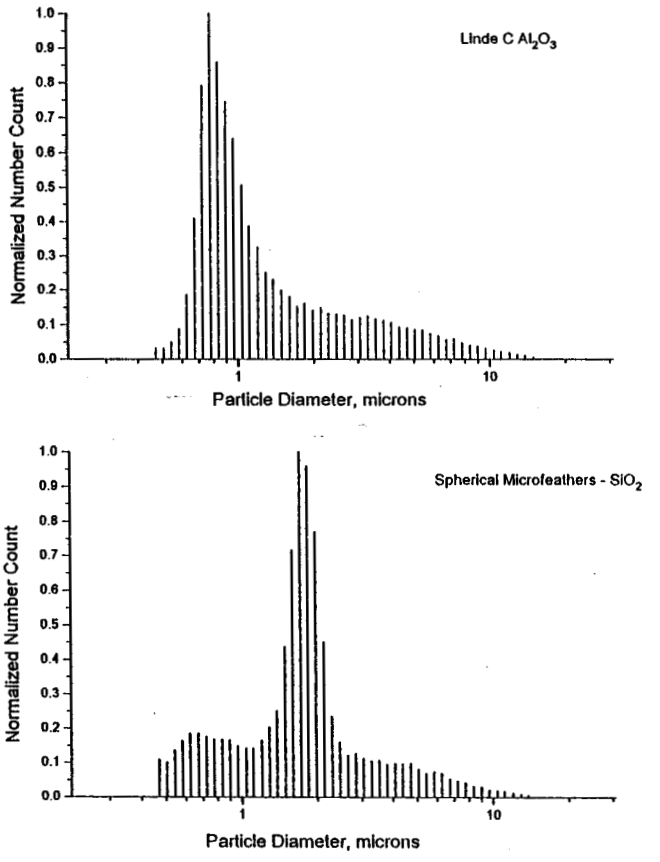

Fig. 2. Normalized aerodynamic particle size distributions, from a TSI APS, for the Linde C Al_2O_3, and hollow spherical SiO_2 "microfeathers."

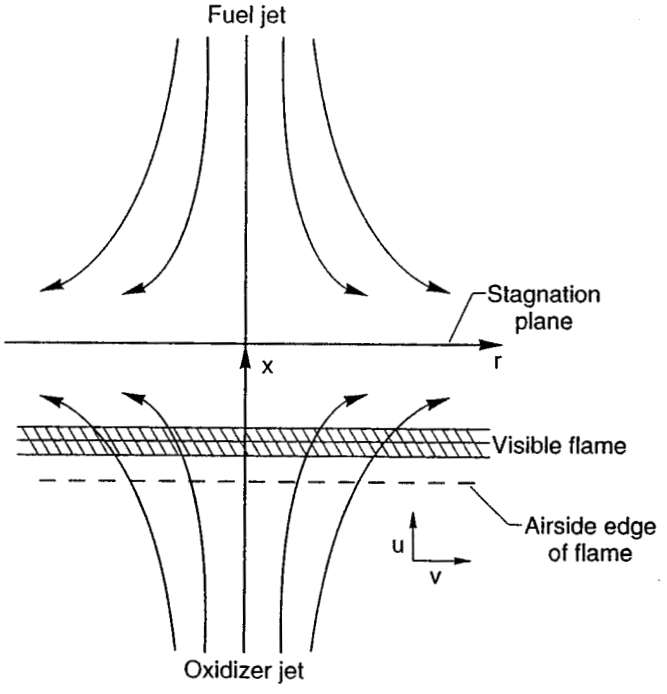

Fig. 1b. Schematic diagram of the axial-radial flowfield of a H_2/N_2–air counterflow diffusion flame.

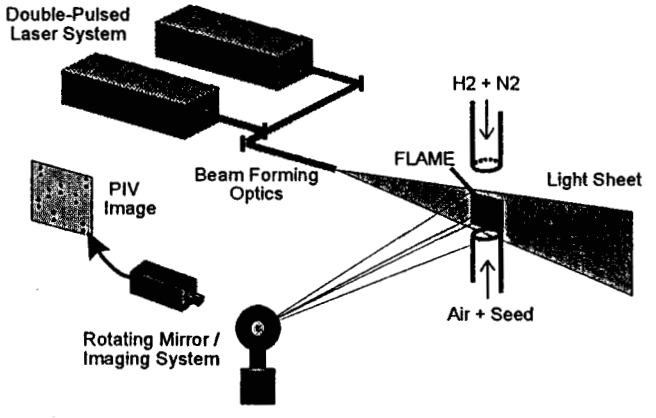

Fig. 3a. Schematic diagram of the Nd-YAG double-pulsed Particle Imaging Velocimetry (PIV) System.

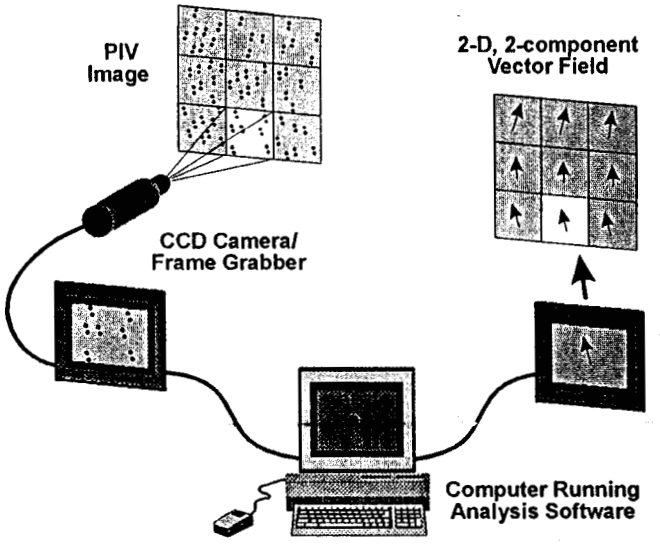

Fig. 3b. Diagram of the PIV image analysis system.

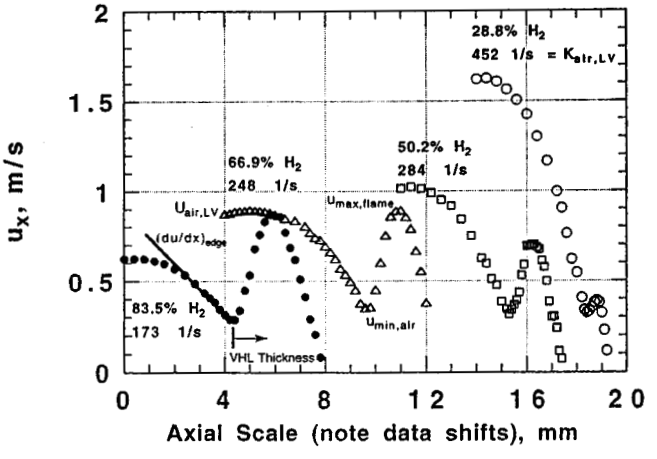

Fig. 4a. High-resolution LDV data for fuel inputs of 1 SLPM H_2 + variable N_2 to a 7.2 mm nozzle OJB. Data apply on centerline of Al_2O_3-seeded airside flow. Note mole percent H_2, and input axial strain rate estimated from LDV velocity input, $K_{air,LV} = 2U_{air,LV} / D_n$.

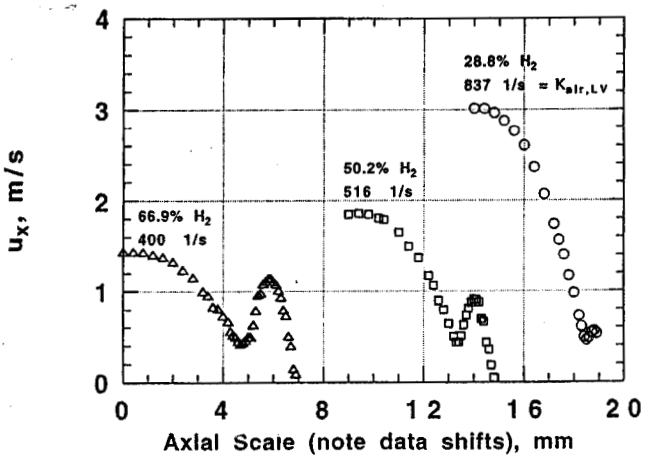

Fig. 4b. High-resolution LDV data for fuel inputs of 2 SLPM H_2 + variable N_2 to 7.2 mm nozzle OJB.

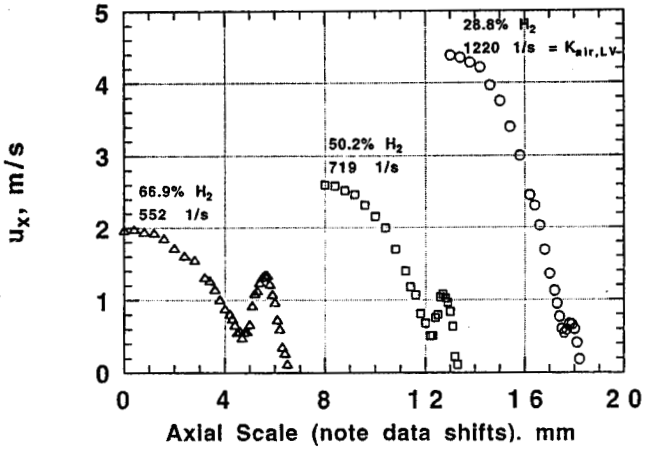

Fig. 4c. High-resolution LDV data for fuel inputs of 3 SLPM H_2 + variable N_2 to 7.2 mm nozzle OJB.

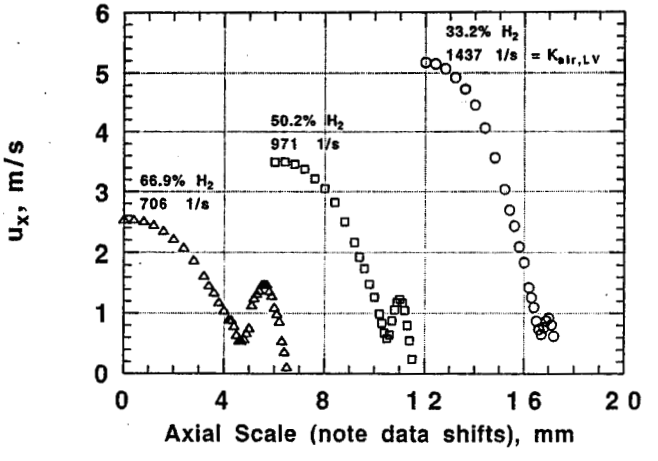

Fig. 4d. High-resolution LDV data for fuel inputs of 4 SLPM H_2 + variable N_2 to 7.2 mm nozzle OJB.

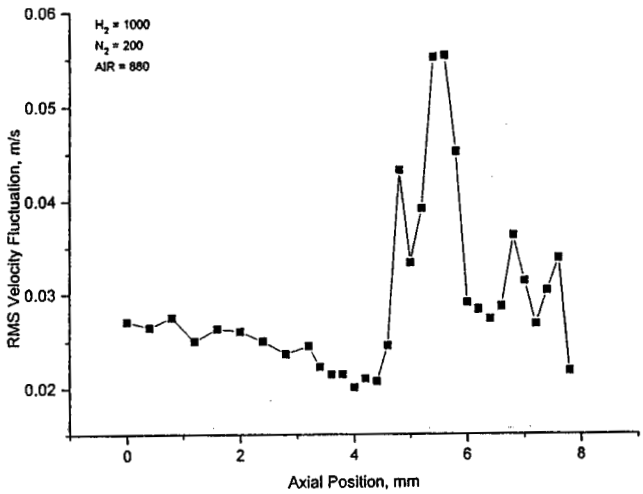

Fig. 5a. Axial distribution of LDV-measured RMS velocity fluctuations; 83.5% H_2, 173 1/s case, Fig. 4a.

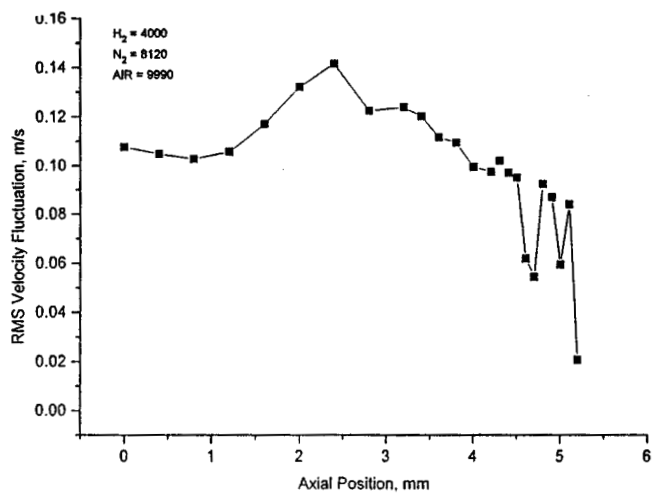

Fig. 5b. Axial distribution of LDV-measured RMS velocity fluctuations; 33.2% H_2, 1437 1/s case, Fig. 4d.

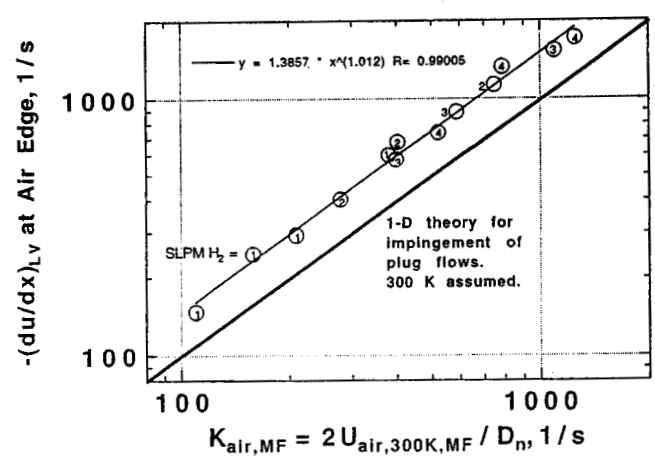

Fig. 6a. **High**-resolution LDV-measured axial strain rates near airside edge of H_2/N_2–air CFDF, using 7.2 mm nozzle OJB. Input axial strain rate was estimated using **mass-flow-derived** air velocity at 300 K.

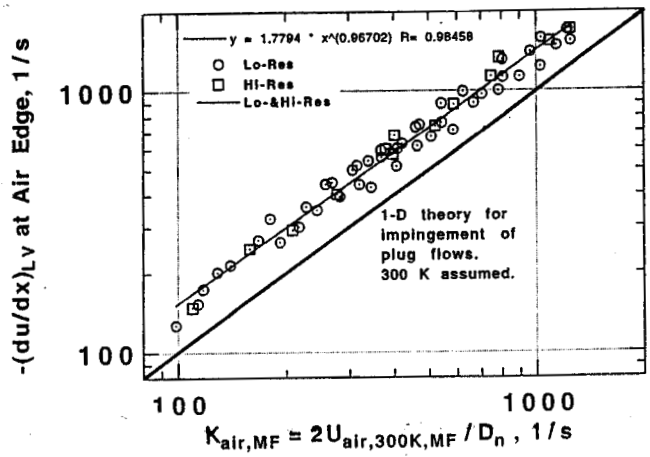

Fig. 6b. **High- and low**-resolution LDV-measured axial strain rate near airside edge, using 7.2 mm nozzle OJB. Input axial strain rate was estimated using **mass-flow-derived** air velocity at 300 K.

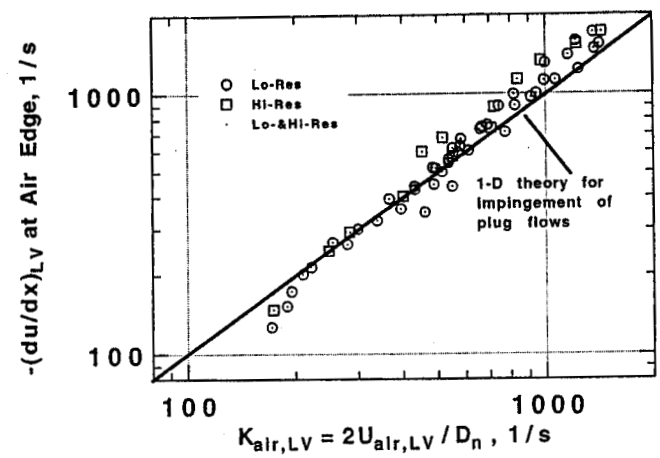

Fig. 6c. **High- and low**-resolution LDV-measured axial strain rate near airside edge, using 7.2 mm nozzle OJB. Input axial strain rate was estimated using **LDV-derived** air velocity.

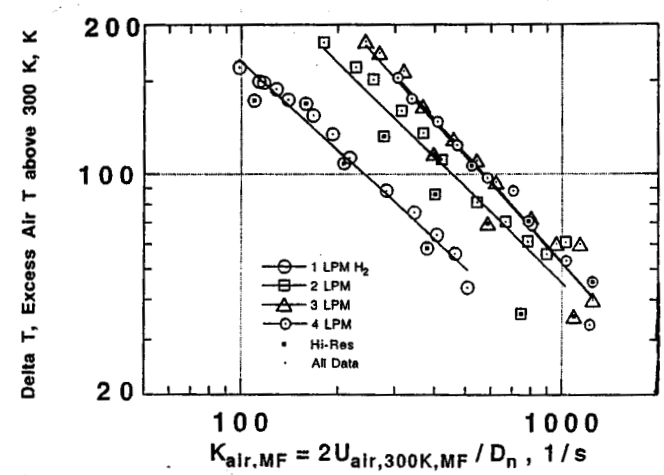

Fig. 7. Implied excess input air temperature, above 300 K, due to convective heating of 7.2 mm air nozzle, for all high- and low-resolution LDV runs. Deduced by equating mass-flow-derived average input velocity to LDV-derived input velocity.

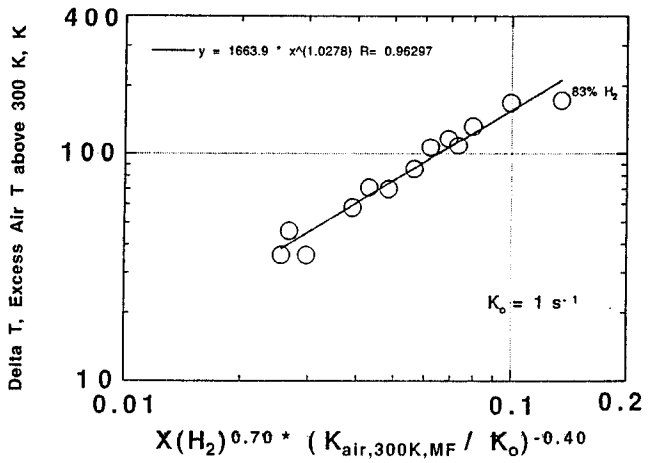

Fig. 8a. Master correlation of implied excess input air temperature, due to convective heating of 7.2 mm air nozzle, for **high**-resolution LDV runs in Figs. 6a and 7.

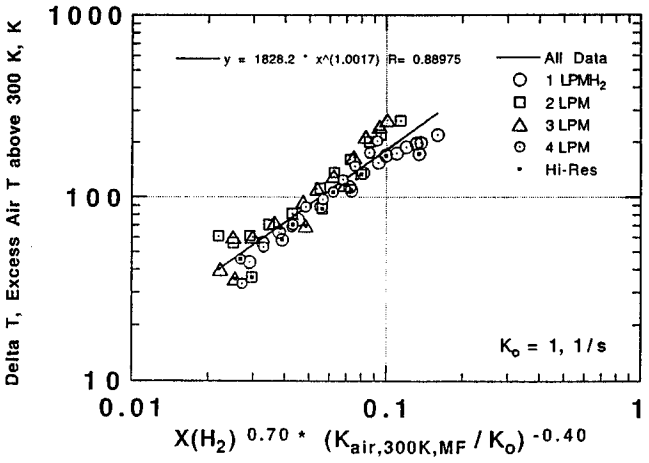

Fig. 8b. Application of master correlation of implied excess input air temperature, tested in Fig. 8a, to both **high and low** resolution LDV runs.

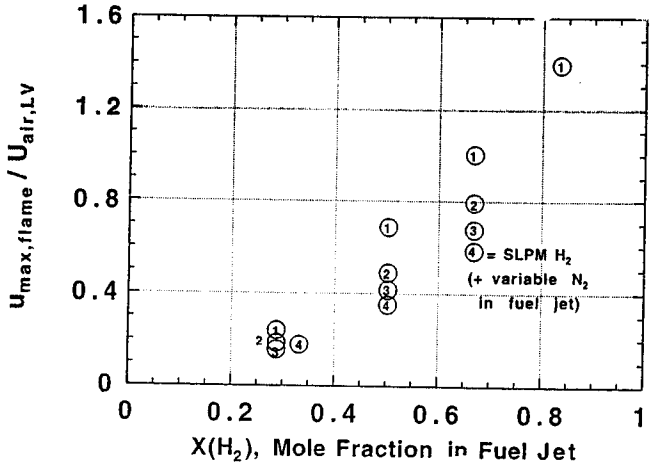

Fig. 9a. Correlation of LDV-derived maximum axial velocity in flame zone, relative to air input velocity. Data from high-resolution LDV, 7.2 mm nozzle OJB.

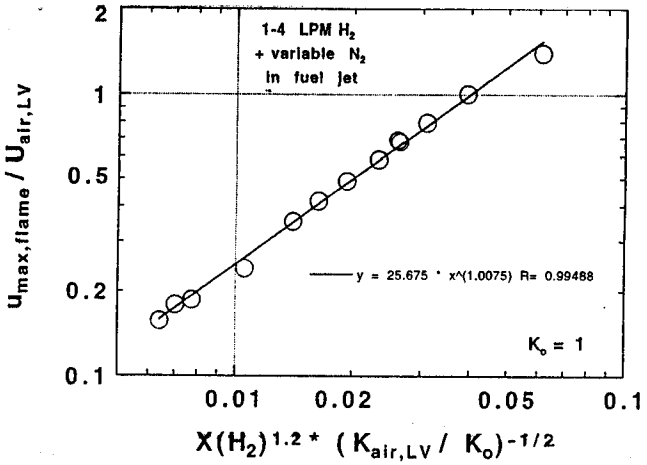

Fig. 9b. Master correlation of LDV-derived maximum axial velocity in flame, relative to air input velocity. Data from high-resolution LDV, 7.2 mm nozzle OJB.

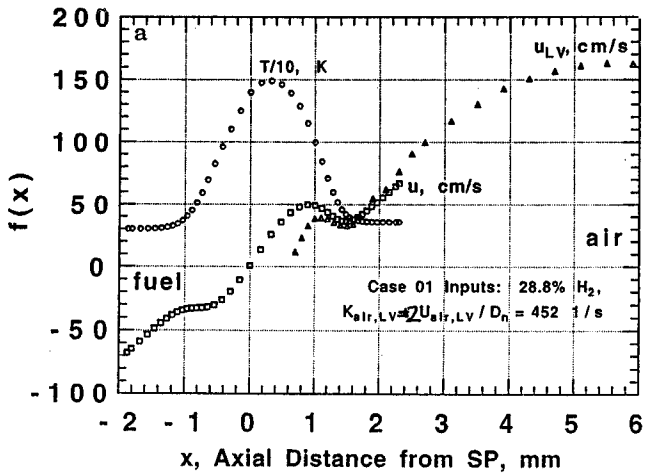

Figs. 10a-e. Example 1-D numerical results, *and* high-resolution LDV data aligned axially at the airside-edge minimum, for a range of input H_2 concentrations and input axial strain rates, defined by air input velocity.

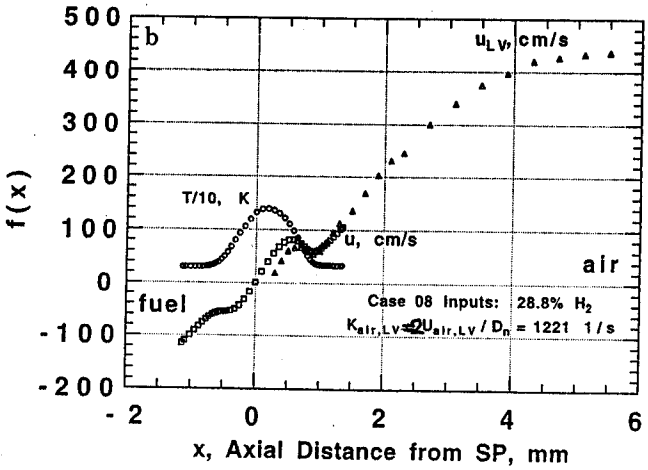

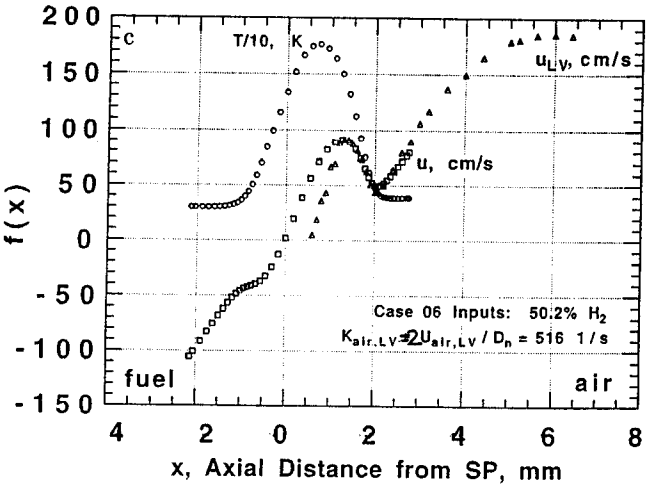

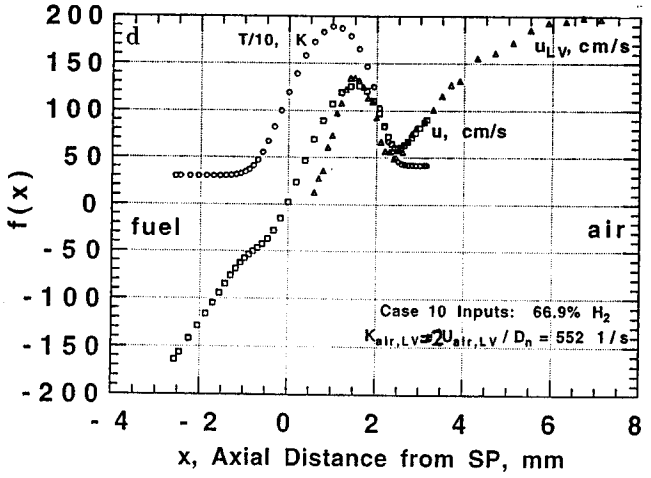

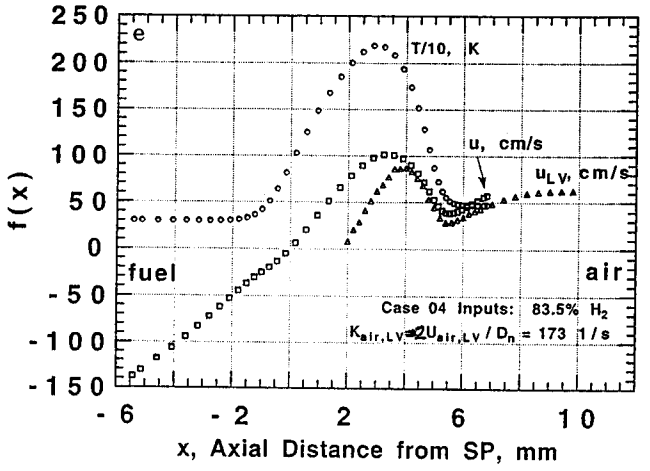

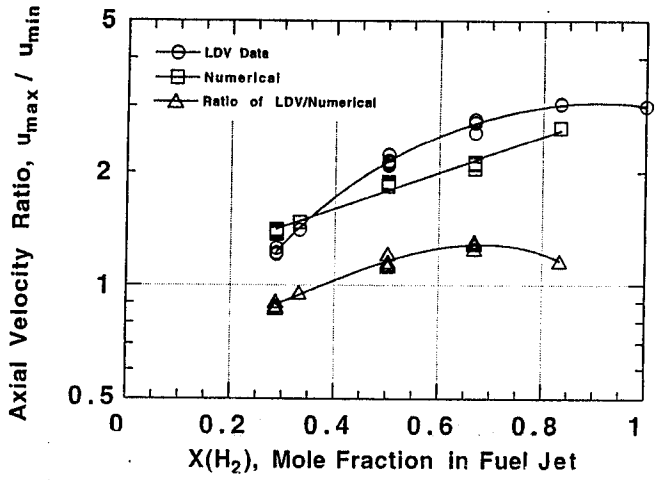

Fig. 11. Ratio of maximum axial velocity in flame zone, to minimum axial velocity near airside edge. For high-resolution LDV data, 7.2 mm nozzle OJB, and 1D numerical results based on same air input velocities.

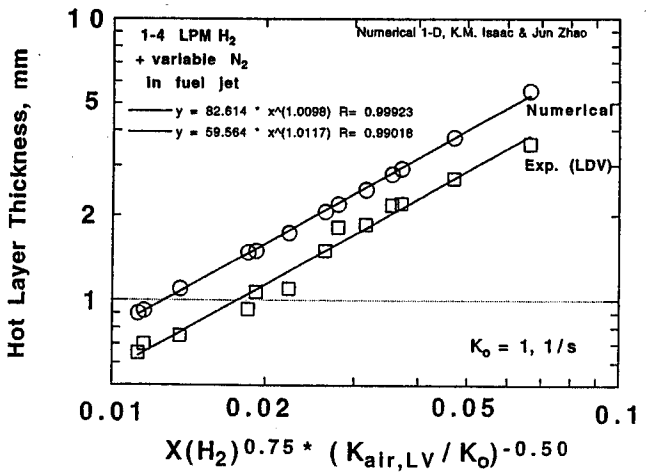

Fig. 12. Master correlation of Velocity Hot Layer thickness. For high-resolution LDV data, 7.2 mm nozzle OJB, and 1-D numerical results.

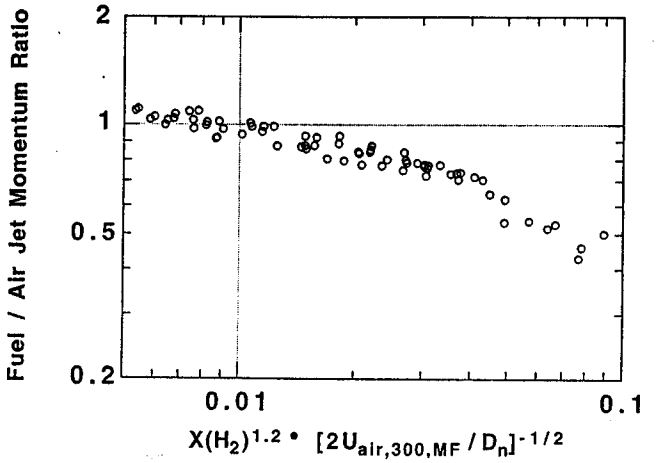

Fig. 13. Correlation of Fuel / Air axial jet momentum ratio for all PIV and LDV, 7.2 mm nozzle-OJB flows.

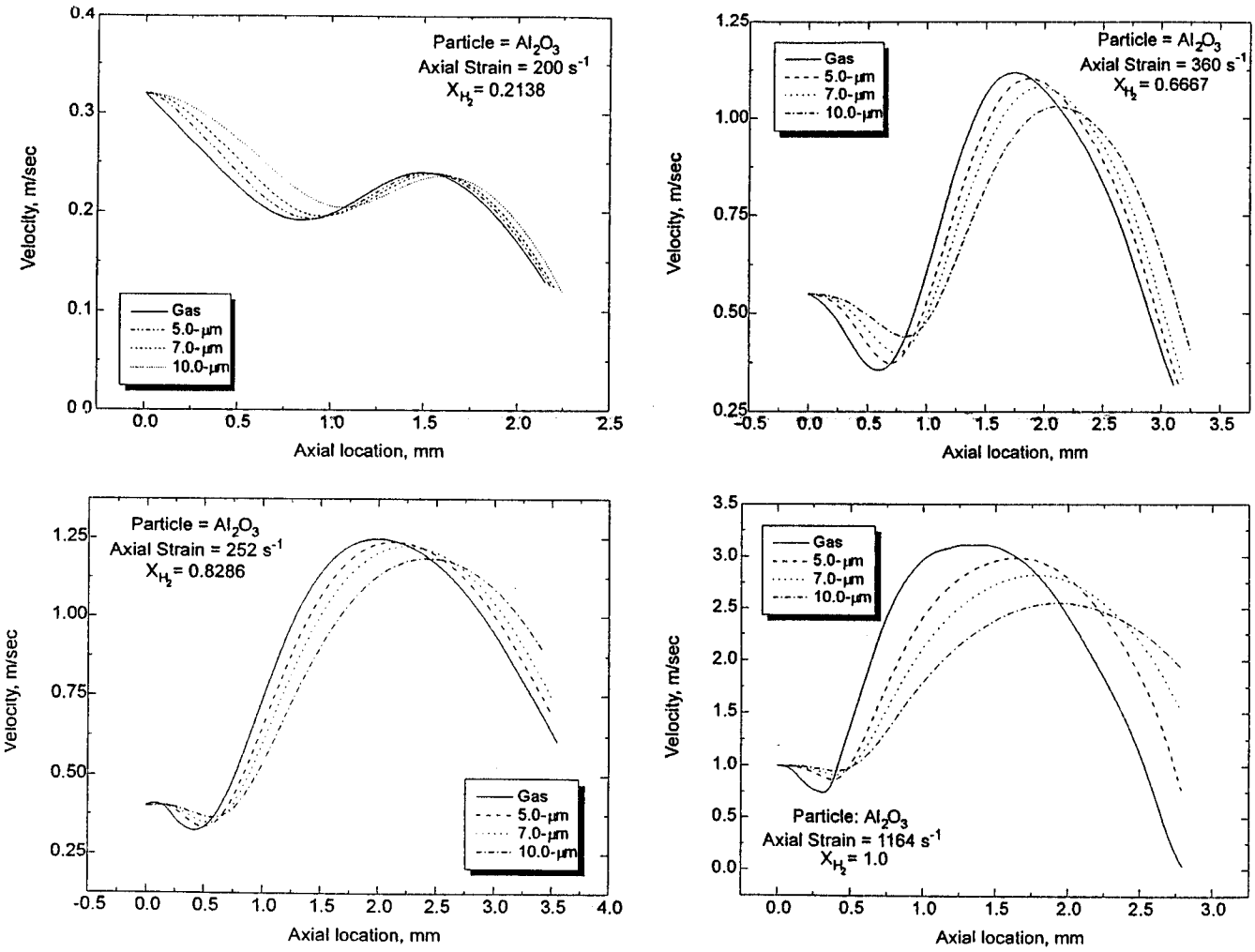

Fig. 14a. Calculated particle-lag effects for 5, 7, and 10 micron solid **Al_2O_3**, for four widely-varied sets of input H_2 concentrations, and airside axial strain rate inputs.

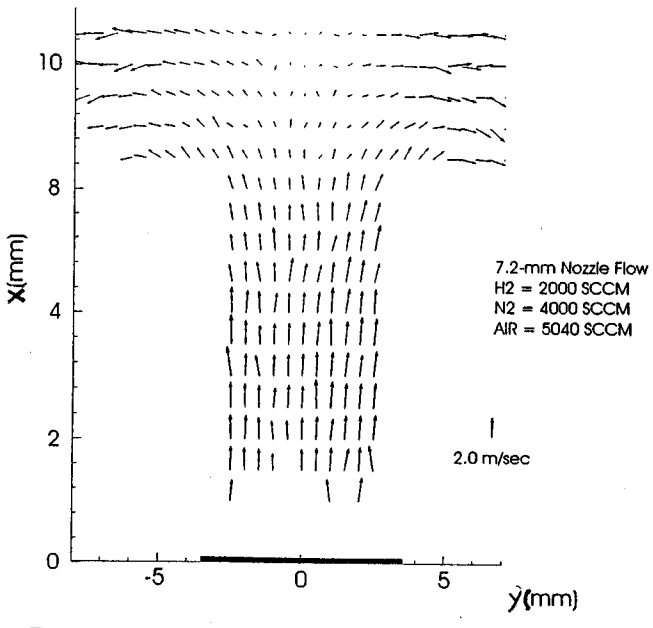

Fig. 15a. Typical vector plot derived from PIV measurements, using 7.2 mm nozzle OJB, 33% H_2 input, and Linde C Al_2O_3 seed.

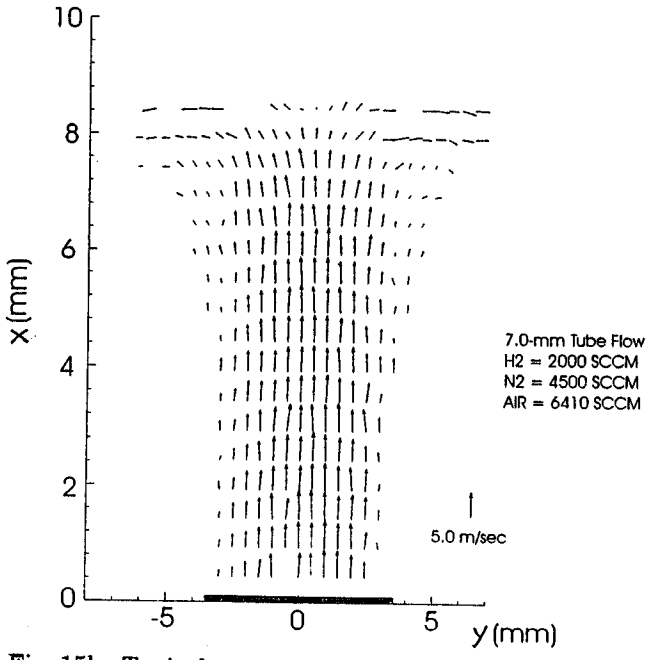

Fig. 15b. Typical vector plot derived from PIV measurements, using 7.0 mm tube OJB, 31% H_2 input, and hollow SiO_2 microsphere seed.

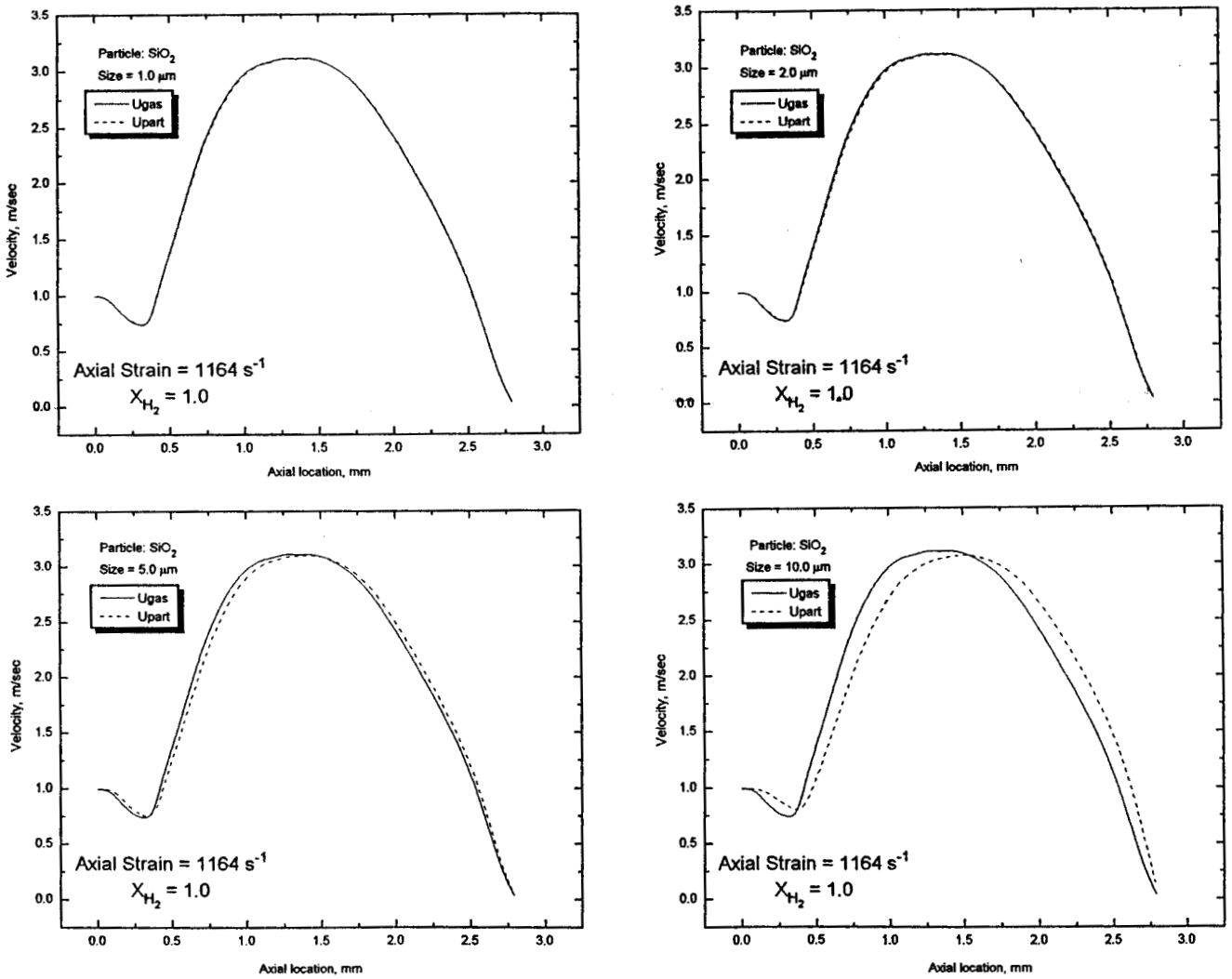

Fig. 14b. Calculated particle-lag effects for 1, 2, 5, and 10 micron hollow **SiO_2** microspheres, at a relatively-high airside axial strain rate input, using 100% H_2 fuel.

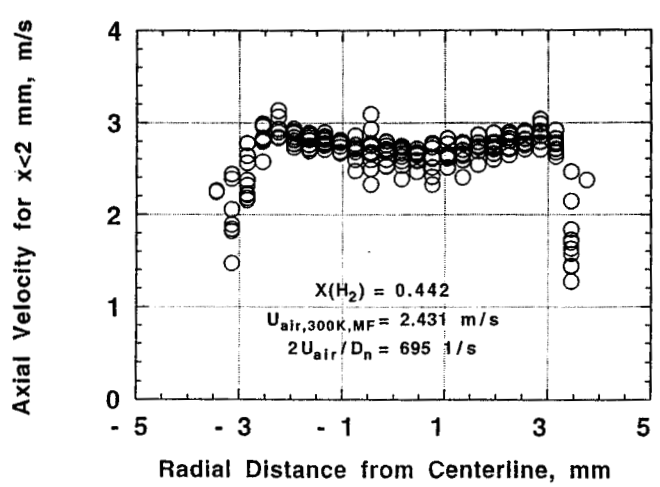

Fig. 16a. PIV-determined initial radial profile of axial input air velocity, **7.2 mm nozzle** OJB, Al_2O_3 seed.

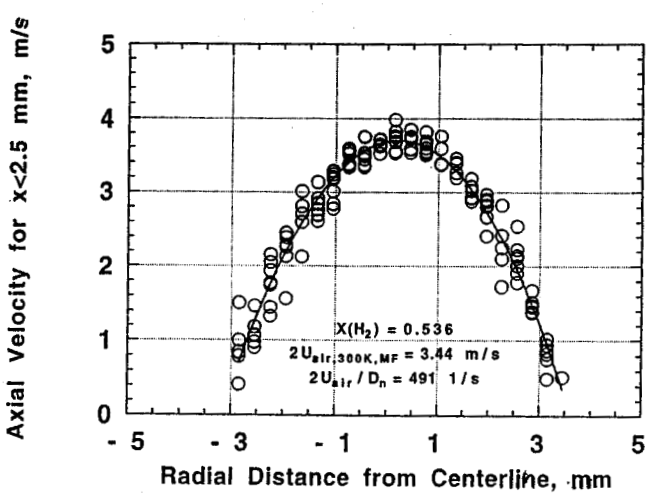

Fig. 16b. PIV-determined initial radial profile of axial input air velocity, **7.0 mm tube** OJB, Al_2O_3 seed.

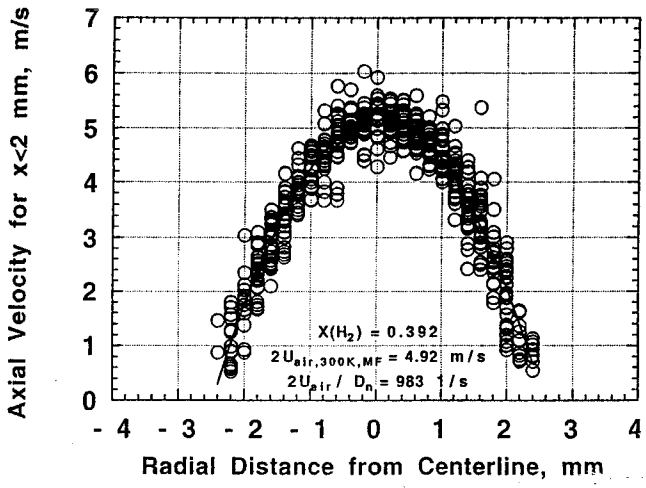

Fig. 16c. PIV-determined initial radial profile of axial input air velocity, **5.0 mm tube** OJB, Al_2O_3 seed.

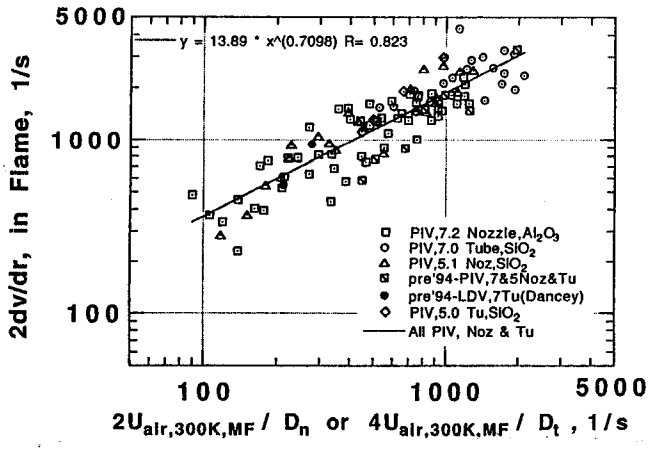

Fig. 17c. Summary of PIV-measured **radial velocity gradient in the flame.** The abscissa represents estimated input axial strain rate based on mass-flow-derived input air velocity, OJB type, and jet exit size.

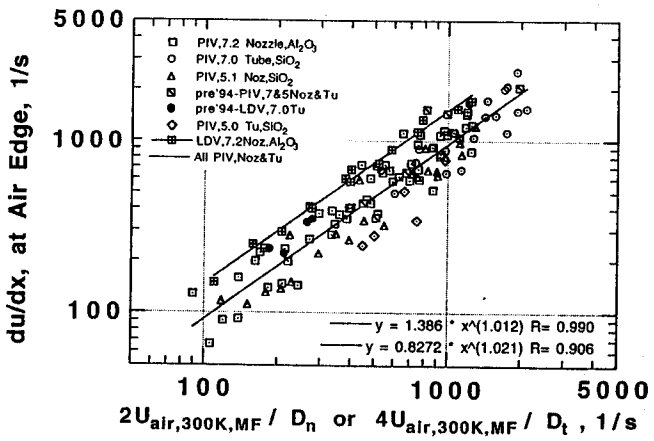

Fig. 17a. Summary of PIV- and LDV-measured **axial strain rate near the airside edge** of the flame; for both 7 and 5 mm nozzle- and tube-OJBs, and Al_2O_3 and hollow SiO_2 seeds. The abscissa represents input axial strain rate, estimated for nozzles *or* tubes, using **mass-flow-derived** input air velocity at 300 K.

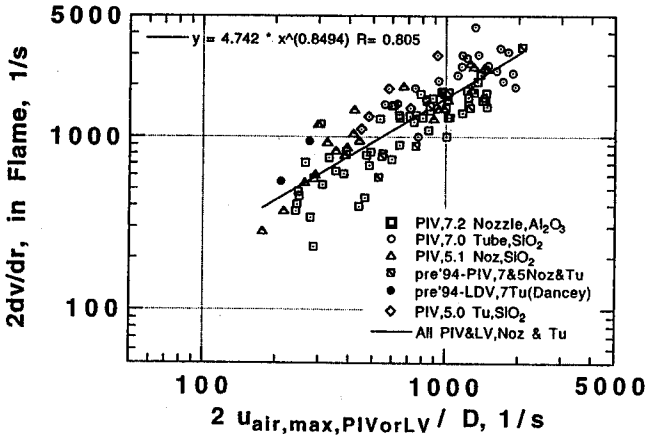

Fig. 17d. Same data as in Fig. 17c, *except* abscissa is based on **PIV- and LDV-measured** input air velocity.

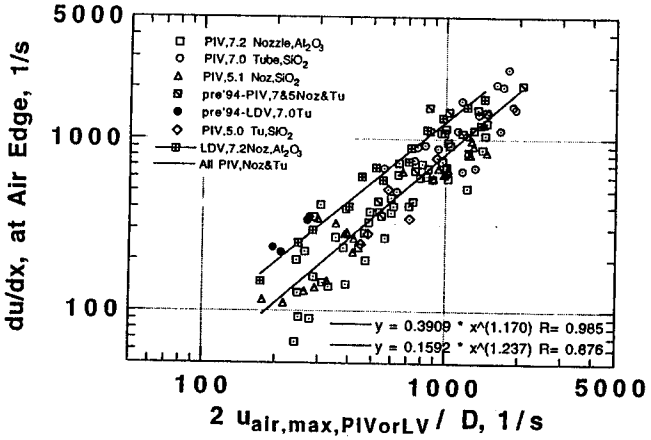

Fig. 17b. Same data as in Fig. 17a, *except* abscissa is based on **PIV- and LDV-measured** input air velocity.

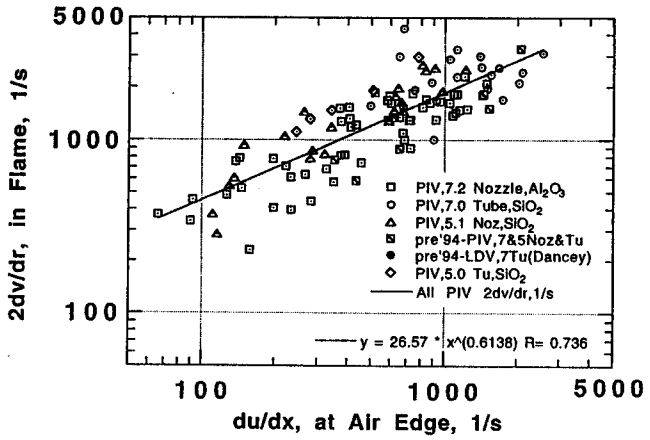

Fig. 17e. Summary of PIV-measured **axial strain rate** crossplotted **versus radial velocity gradient in the flame.**